
Spectroscopy of momentum-dark excitons in layered semiconductors

Spektroskopie von impuls-dunklen Exzitonen in Dünnschicht-Halbleitern

VICTOR FUNK



Munich, August 2017

Spectroscopy of momentum-dark excitons in layered semiconductors

*Spektroskopie von impuls-dunklen Exzitonen
in Dünnschicht-Halbleitern*

MASTER THESIS

Submitted by

Victor Funk

born in Schwäbisch Gmünd

at

Faculty of Physics

Solid state physics

Prof. Dr. Alexander Högele

Ludwig–Maximilians–Universität Munich

Munich, August 1, 2017

Review by:
Prof. Dr. Alexander Högele
Michael Förg

Layered semiconductors of transition metal dichalcogenides (TMD) show a crossover from an indirect to a direct bandgap when the number of layers is reduced from a bulk crystal down to a monolayer. Two-dimensional TMD monolayers have a weak dielectric screening and therefore strong Coulomb interactions, forming tightly bound excitonic states. The strong optical response in the visible regime induces attractive applications of TMD monolayers in photonic devices. Due to the high surface-to-volume ratio, the dielectric environment has an intense impact on optical signatures. The linewidths of the free excitons exhibit significant inhomogeneous broadening, attributed to the influence of the substrate. Cryogenic photoluminescence spectroscopy of encapsulated TMD monolayers in hexagonal boron nitride recently showed a reduction of the spectral linewidth towards the radiative limit. Due to the encapsulation, substrate effects on TMD monolayers are excluded from the emission spectra. With the resolution of the sub-peak structure, open questions regarding the physical origin are accessible. In this work, heterostructures of TMD monolayer and hexagonal boron nitride were fabricated with exfoliation and transfer methods and subsequently characterized with cryogenic photoluminescence spectroscopy. In order to understand the resulting spectral signatures, a model was introduced which includes radiative recombination of spin-bright and spin-dark momentum-direct excitons as well as momentum-dark excitons. The ladder refers to optically forbidden intervalley excitons, where the hole is located at the K point of the valence band and the electron either at the K' or Q point of the conduction band. Electron-phonon scattering changes the net momentum of the momentum-dark excitons and enables a radiative contribution from these states, referred to as phonon replicas. Optical signatures of momentum-dark excitons are identified in tungsten based TMD monolayers, where the analysis extracts the relative energetic position of the Q point with respect to the lowest lying energetic spin-dark state. The analysis of an encapsulated monolayer of molybdenum diselenide challenge the contribution of the trion state to the spectral signatures.

Contents

1	Introduction	1
2	Fundamentals of layered semiconductors	3
2.1	Real space lattice of transition metal dichalcogenides	3
2.2	Electronic bandstructure	4
2.3	Momentum-dark excitons	8
2.3.1	Phonons	8
2.3.2	Phonon sideband model	9
3	Sample fabrication and characterization	13
3.1	Mechanical methods	13
3.1.1	Exfoliation of two dimensional crystals	13
3.1.2	Hexagonal boron nitride	16
3.1.3	Transfer by viscoelastic stamping	17
3.2	Optical setup	19
3.3	Layernumber quantification	20
3.3.1	Raman spectroscopy	22
3.3.2	Photoluminescence-imaging	23
3.3.3	Optical contrast	26
3.4	Sample characterization with photoluminescence-imaging . . .	27
3.4.1	Silver substrates	27
3.4.2	Annealing	29
4	Spectroscopy of tungsten based transition metal dichalcogenides	31
4.1	Encapsulated samples	31
4.2	Monolayer on hexagonal boron nitride	35
5	Spectroscopy of encapsulated molybdenum diselenide	39
6	Summary and outlook	43
	Bibliography	45

List of Figures

2.1	Real space lattice of transition metal dichalcogenides	4
2.2	Bandstructure of of transition metal dichalcogenides	5
2.3	Valley model for transition metal dichalcogenide monolayer . .	7
2.4	Real space vibrational modes in transition metal dichalcogenide monolayers	9
2.5	Phononic dispersion relation and scattering processes	10
2.6	Phonon sideband model for transition metal dichalcogenide mono- layers	11
3.1	Exfoliation of van der Waals crystals	14
3.2	Hexagonal boron nitride	17
3.3	Stamping stage	18
3.4	Transfer process	19
3.5	Optical setup	21
3.6	Raman spectroscopy	23
3.7	Photoluminescence comparison of transition metal dichalcogenide monolayers at room-temperature	24
3.8	Layer number quantification of few-layer transition metal dichalco- genides	25
3.9	Optical contrast analysis	27
3.10	Silver substrates and enhancement effects	28
3.11	Annealing process	30
4.1	Emission spectra of encapsulated WSe ₂ and WS ₂	32
4.2	Emission spectra of WSe ₂ and WS ₂ monolayer on hexagonal boron nitride	35
4.3	Quantum dot emission	37
5.1	Emission spectra of encapsulated MoSe ₂	39

Introduction

In 2010, the Nobel prize in physics went to Andre Geim and Konstantin Novoselov for groundbreaking experiments regarding the two-dimensional (2D) material graphene. The isolation of graphene from its bulk crystal graphite was thereby achieved with the so-called "Scotch-Tape method". Roughly speaking, it's playing with a pencil and a stripe of tape. Strong covalent in-plane bonds and weak out-of-plane Van-der-Waals forces enable exfoliation of bulk crystals to the monolayer (ML) form [19]. Subsequent to graphene, a variety of 2D materials with similar hexagonal crystal structure were studied in their single-layer form, where new physical phenomena arise from the change of dimensionality.

A prominent class of layered semiconductors are transition metal dichalcogenides (TMD), which show unique optoelectronic properties in the limit of single unit cell thickness [36]. A striking property of these materials is the crossover from an indirect-gap semiconductor at multilayers to a direct bandgap at the monolayer limit, resulting in strong photoluminescence [4, 39]. Weak dielectric screening in TMD MLs due to the high surface-to-volume ratio enables strong Coulomb forces between optically excited electrons and residual holes. These form tightly bound excitonic states with electric field lines exceeding the spatial extension of the crystal [14].

This outlines the strong impact of the dielectric substrate on the excitonic states related to optical signatures. The observed spectral linewidths of the excitons exhibit significant inhomogeneous broadening which is typically attributed to the local spatial inhomogeneity of the substrate, residual molecules on the surface and different doping and dielectric screening conditions [37]. Hexagonal boron nitride (hBN) was found to exclude such effects by providing an electrostatic stable dielectric environment with a smooth and homogeneous surface.

This work addresses the optical properties of few-layer crystals of MoS_2 , MoSe_2 , WS_2 and WSe_2 . Exfoliation methods, together with the deterministic transfer technique of viscoelastic stamping [12] were used to fabricate heterostructures of TMD monolayers and hBN which were subsequently characterized with cryogenic photoluminescence spectroscopy.

Recent publications reported on emission spectra of encapsulated TMD monolayers in hBN, showed a reduction of the spectral linewidth towards the radiative limit [1, 7]. The increased resolution of the peak structure enables a more profound investigation of the radiative processes involved.

The role of phonon assisted optical transitions has recently been demonstrated for hBN, where the nature of its indirect bandgap was resolved with the inclusion of phonon replicas [10]. However, theoretical bandgap calculations and further analysis of optical transition rules proposed momentum-dark (indirect) excitonic states in TMDs [32, 35]. Radiative recombination of the momentum-dark excitons occur via an electron-phonon scattering mechanism. In this work, a model is introduced which interprets all spectral signatures of TMD MLs in the context of phonon sidebands [2].

This thesis begins with a revision of the fundamental properties of TMD MLs. A phonon sideband model is then proposed in chapter 2.3. Following this, the fabrication and characterization methods used to build and examine heterostructures of TMD monolayers and hBN are shown in chapter 3. In chapter 4, the model was applied to cryogenic optical signatures of tungsten based TMDs encapsulated in hBN, as well as on MLs transferred on top of hBN. The expansion of the model to encapsulated MoSe₂ is then shown in chapter 5 and finally, a brief summary and an outlook are given in chapter 6.

Fundamentals of layered semiconductors

With the successful exfoliation of graphene from usual bulk graphite, a new field of research quickly developed and extended to many different materials. The vanishing bandgap in graphene motivated extensive studies of novel layered semiconducting materials. Transition metal dichalcogenides (TMDs) are one prominent example, where the physical properties are dramatically changing, when reaching a monolayer (ML) form. TMDs show unique optical properties which are studied in this thesis. [24, 39]

2.1 Real space lattice of transition metal dichalcogenides

Similar to graphite, TMD bulk material consists of atomic monolayers stacked on top of each other. Van der Waals forces weakly bind the layers whereas strong covalent bonds within the layer define the atomic structure.

Shown in figure 2.1 (a) is a schematic drawing of the atomic configuration of TMDs. Transition metals such as molybdenum (Mo)- and tungsten (W)-atoms (black) are encapsulated by chalcogenide atoms (X) of sulfur (S) or selenium (Se) (yellow). Disregarding TMDs with the chalcogenide tellurium or other transition metals, four possible molecular combinations arise: MoS_2 , MoSe_2 , WS_2 and WSe_2 .

The atomic structure is identical in first order treatment. Each transition metal is coordinated by six neighbouring X atoms in a trigonal prismatic geometry and exhibits a hexagonal two atom based crystal structure (Figure 2.1 (b) and (c)). The crystal symmetry in a ML reduces to D_{3h}^1 : the trigonal prismatic geometry is invariant under 3-fold rotations and exhibits an additional horizontal reflection plane.

Interestingly, the inversion symmetry is broken: when the transition metal atom is taken as the inversion center of the unit cell, an X atom is mapped onto an empty location. This is a fundamental difference to graphene and gives rise to spin valley physics, discussed in section 2.2. [36, 39]

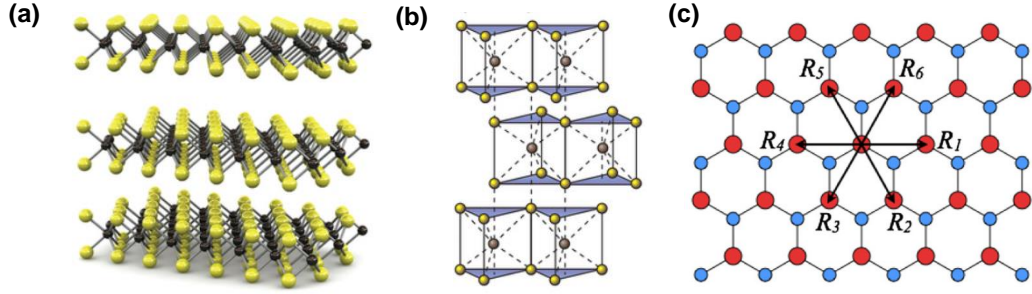


Figure 2.1: **(a)** Schematic drawing of the atomic configuration in TMDs. Black dots represent the transition metal atoms, encapsulated by chalcogenide atoms in yellow. Strong covalent bonds define the crystal structure of each layer. Van der Waals forces between the layers are forming the three dimensional crystal. **(b)** Trigonal prismatic unit cell, with the metal atom in the center and six nearest neighbours of chalcogenites. An exemplary 2H stacking is depicted. **(c)** Alternating arrangement of the metal- (red) and the chalcogenides-atoms (blue) from the top view, forming a hexagonal crystal structure. Arrows indicate the six nearest neighbours of the metal atom in the center. Graphics taken from [36, 39].

2.2 Electronic bandstructure

The bandstructure of semiconducting TMDs is dominated by the d-orbitals of the transition metals with $l = 2$. These orbitals hybridize with the p-orbitals of the chalcogenides atoms [36], giving rise to a finite bandgap. For bulk crystal, the lowest lying conduction band (CB) and the highest valence band (VB) are momentum indirect at the Γ point of the VB. For ML-TMDs this changes due to the reduced spatial extension of the crystal, leading to confinement effects on the orbitals. The resulting bandstructure exhibit a direct transition at the K-point, as shown in figure 2.2 (a). [9, 20, 36]

The sixfold symmetry of the unit cell in real space results in a hexagonal Brillouin zone. The VB arises from the $d_{x^2-y^2}$ and d_{xy} orbitals of the metal atom. The inversion symmetry breaking induces an opposite sign in the magnetic quantum

numbers (m_j) of the hybridized orbitals on alternating K points in the VB. Spin orbit coupling (SOC) leads to a splitting of these highest energetic states in opposite directions: For the K point, commonly referred to as K valley, the spin-up state is energetically higher than the spin-down state. In the alternating -K valleys (also labeled as K'), the energetic ordering of the spin states is reversed. A schematic depiction is shown in figure 2.2 (b). [9]

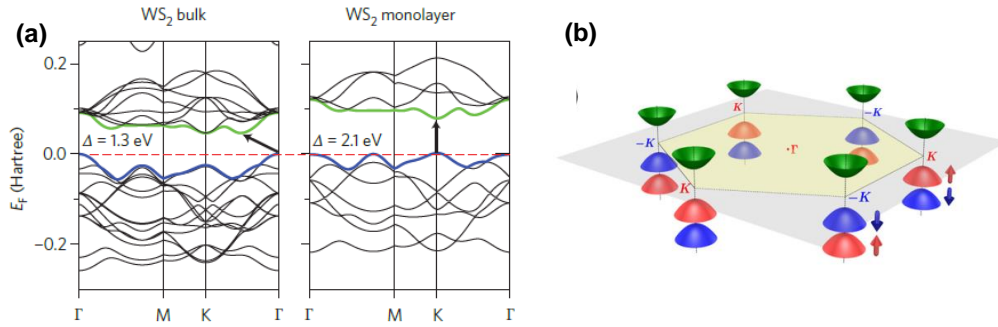


Figure 2.2: **(a)** Bandstructure of WS_2 in bulk (left) and monolayer (right). The energetic lowest CB / highest VB is indicated in green / blue. The Fermi-level is shown by a red line and represents the electron occupation at the energetic ground state. The bandstructure changes from a momentum-indirect transition at the Γ -point in bulk, to a direct transition at the K-point in the monolayer. **(b)** Schematic drawing of the hexagonal first Brillouin zone of MoS_2 . The band edges are located at the K points. The VB and the CB approximately show a quadratic dispersion relation. SOC and inversion symmetry breaking lead to a splitting of the two highest energetic VB states, with alternating spin directions for the energetically higher VB, labeled as the K and -K valleys respectively. Graphics taken from [36, 39].

The density functional theory (DFT) calculations associated with figure 2.2 (b) neglect effects of the SOC in the CB. The assumption that d_z with $l=0$ defines the CB is reasonable for the case of MoS_2 . Hereby the CB K-valley is two-fold spin degenerate, with $m_j = +3/2$, $m_j = +1/2$ as well as negative signs for K' [6]. However, when additional orbitals from the chalcogen atoms are taken into account, more recent calculations show that this degeneracy is lifted for all four TMDs examined in this work. In the case of tungsten based TMDs, even the ordering of the CB spin states changes and gives rise to a so called "dark-state". [22, 26]

Optical selection rules dictate the transitions between the CB and VB. For dipolar emissions, momentum direct recombinations with $\Delta m_j = \pm 1$ lead to an emission of circularly polarized light. The K and K' valleys emit right (σ_+)- and left-handed (σ_-) circularly polarized light respectively, perpendicular to the ML.

By tuning the polarization of the excitation, the population of charge carriers in the valleys can be controlled. This unique property is commonly referred to as circular dichroism and gives rise to an additional valley degree of freedom. Circularly polarized light only populates one valley (K or K'), whereas linearly polarized light couples to both valleys as it is a superposition of left and right-handed circular light. [9]

The spin ordering in the CB differs for tungsten based TMDs. The spins of electrons in the lowest lying CB at the K (K') point have anti-parallel spin compared to electrons in the highest VB. If $\Delta m_j = 0$, emission of out of plane circularly polarized light is forbidden due to momentum conservation. This is referred to as (spin-) dark state. The bright-dark energy splitting was recently experimentally determined via spectroscopy at very high magnetic fields, or by excitonic coupling to surface polaritons, resulting in values of 40-47 meV for WSe₂ and 47-55 meV for WS₂ [35, 44, 47]. For a full description, optical transition rules have to be derived from group theoretical analysis of the crystal symmetry [17, 35]. The resulting dark-state emission is in-plane with the ML and has a linear polarization. As the dark state is energetically more favorable, DFT calculations predict a higher carrier population on the order of $\sim 10^3$, compared to the upper, spin bright state. Experimentally, the dark-state shows a high intensity peak for in-plane excitation and detection, but is also observable for an out-of-plane excitation and collection of light [35]. Objectives with a high numerical aperture (NA) have a large collection-angle, such that a significant component of the in-plane radiation is captured even with out-of-plane excitation and detection.

An additional local minimum for the lowest CB, nearly half-way between the K and the Γ point, further complicates the model. The so-called Q valley (also referred to as Λ -point), derived from kp-theory, is approximately parabolic around the minimum and exhibits different effective electron masses. It also shows a SOC, which leads to a small correction for molybdenum based TMDs. For tungsten based TMDs on the other hand, SOC in the Q-valley is significant, with values of $\Delta Q \sim 220$ meV for WSe₂ and ~ 260 meV for WS₂. The carrier density needed to populate these valley is reduced by a factor of ~ 5 , compared to the case for molybdenum. [22, 32]

This demands an inclusion of the Q-valley to the band-model, which aims to describe and reproduce spectral signatures obtained in cryogenic environments. A schematic band model in the single particle picture is shown in figure 2.3.

In the case of WSe₂, the Q-valley lies energetically between the bright and dark state, where as for WS₂, the Q valley is energetic higher than the bright state. The small energetic spacing between these states however, indicates a strong

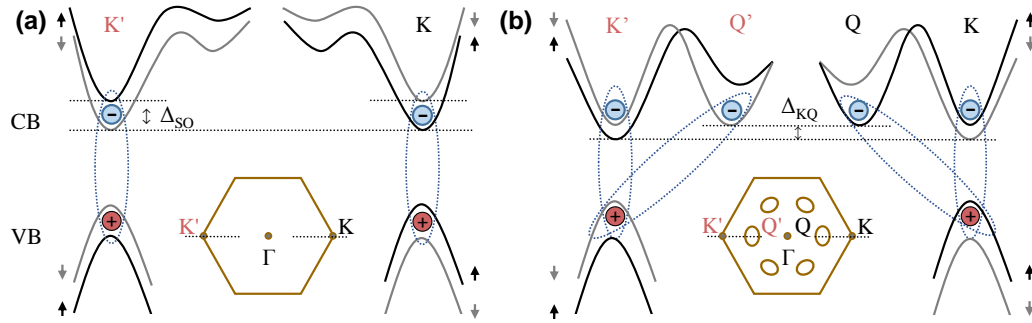


Figure 2.3: **(a)** Schematic band structure of molybdenum dichalcogenides. Excited electrons and residual holes form a bound state due to strong coulomb interactions. SOC and broken inversion symmetry result in momentum-direct exciton emission from the K and K'-valleys, with polarization according to the residual valleys. The population of the Q-valley is neglected. The energetic spacing of the two highest VB states is reduced for clarity. The first Brillouin zone is depicted for clarity between K and K'. **(b)** Schematic band-structure for tungsten based TMDs. The valley spins of the lowest CB are inverted, leading to spin-dark states. In the case of WSe_2 , the Q-valley lies energetically between the bright and dark state, whereas for WS_2 , the Q valley is energetic higher than the bright state. The small energetic spacing between these states however, induces a strong population leading to possible momentum-indirect exciton formations, further discussed in chapter 2.3. Illustration modified from [2].

population. In general, theoretical bandstructure calculations in TMDs including spin-orbit coupling, show varying results. For MoSe_2 , a reported value of the energy separation between the K and the Q-valley amounts to only 28 meV [20] instead of 138 meV [22], which can significantly impact radiative processes.

For optical experiments in semiconducting TMDs, it is mandatory to switch to an excitonic picture. When electrons (e^-) at the K point are excited to the CB, residual holes (h^+) remain in the VB. These form a bound state due to strong coulomb-interactions and are described in the quasi-particle picture of Wannier-Mott excitons. Excitons behave, in first order, like hydrogen atoms with well-defined orbitals and give a finite correction to the band-structure. In ML-TMDs one can solve the Schrödinger equation of a 2D-hydrogen atom with reduced e^- and h^+ masses determined by the curvature of the charge-carrier valley. Assuming a locally screened attractive coulomb interaction gives a good first order approximation. The resulting energy for the ground state reveals the excitonic binding energy E_X . Typical experimental values of E_X for different TMDs are in the range of 100 meV - 700 meV and unfortunately strongly varying in litera-

ture [14, 22, 48]. Fermi's golden rule dictates the lifetime of these bound states. Excitons of ML-TMDs at cryogenic temperatures show a lifetime in the range of pico-seconds [28]. Spontaneous recombination of the e^- and h^+ leads to photon emission, with an energy of: $E_\gamma = E_{gap} - E_X$. This description however, neglects nonuniform dielectric environments leading to a change in effective screening and therefore, to varying exciton energies. [14, 32]

2.3 Momentum-dark excitons

As highlighted in figure 2.3 (b), due to the high population of multiple symmetry points in the first Brillouin zone (K, K', Q, Q'), momentum-indirect exciton formations have to be considered. A direct radiative recombination is forbidden due to momentum conservation, leading to the name momentum-dark exciton. For radiation to occur, a second order process involving a phonon-carrier scattering mechanism is mandatory. Radiative decay of finite-momentum excitons via second order phonon processes was just recently shown for hexagonal boron nitride [10]. This indicates that similar processes occur in TMDs and motivated this work to develop a model in this context. Therefore, phonon properties of TMD monolayer are discussed next, before the model is presented in chapter 2.3.2.

2.3.1 Phonons

As the real space unit cell of ML-TMDs consist of three atoms, $3N - 3 = 6$ possible optical and 3 acoustical vibrational modes arise inside the crystal. These modes are referred to as phonons in the quasi-particle picture of lattice vibrations. Each phonon has a quantized energy $E = \hbar\omega$, dependent on their frequency. A schematic drawing of the possible modes is shown in figure 2.4. The energetic lowest modes are out of plane acoustic (ZA), transverse acoustic (TA) and longitudinal acoustic (LA) modes where all atoms move in phase. In-plane optical modes E'' consist again of longitudinal (L) and transversal (T) modes, where the S / Se atoms vibrate out of phase, while the Mo / W atoms stay static. E' are polar LO and TO modes, with all atoms moving out-of-phase in plane. The energetically higher modes are A''_2 and A_1 optical modes, with an out-of-plane oscillation. The relevant phonon modes for electron-phonon interactions are TA, LA, E' (LO/TO) and A_1 . The contribution from the remaining four branches is found to be negligible due to the weak coupling to charge carriers. [5, 20, 45]

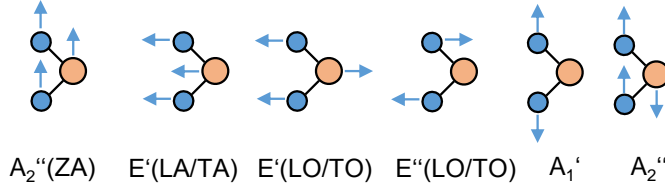


Figure 2.4: Real space representation of possible vibrational modes. Arrows indicate the atomic displacements and their relative phase. The modes are ordered energetically, where the very left acoustical, out-of-plane mode is the energetically lowest. Only the polar modes $E'(LA/TA)$, $E'(LO/TO)$ as well as A_1' are relevant for carrier-phonon interaction [20].

To account for phonon mediated processes with a net-change of momentum, theoretical calculations of the phononic reciprocal space are studied from reference [20]. Figure 2.5 (a) displays the phononic dispersion for the relevant modes in the exemplary case WS_2 . All TMD monolayers show similar behaviour. Figure 2.5 (b) shows possible inter-valley scattering processes for the e^- located at the K point of the first Brillouin zone. The h^+ is thereby fixed at the K point in the upper VB. The arrows mark the allowed e^- transitions K-Q, K-Q' and K-K', all mediated by e^- -phonon scattering processes. Figure 2.5 (c) displays the case with the e^- located at the Q valley, with allowed transitions Q-Q', Q-K and Q-K'. The vertical colour bar denotes the electron energy with respect to the CB band minimum. The table in 2.5 (d) shows the phonon energies for the relevant modes at high symmetry points. All graphics are taken from [20].

2.3.2 Phonon sideband model

For a radiative recombination of momentum-dark excitons to occur, the absolute value of the wave-vector k_{phonon} has to match the momentum difference between the e^- and h^+ , $\Delta k_{e^-/h^+}$ such that the total momentum difference

$$\Delta k = \Delta k_{e^-/h^+} - k_{phonon} = 0$$

As an example, the case is considered where the e^- lies in the Q-valley of the CB and the h^+ in the K valley of the VB. A phonon with momentum K-Q scatters at the e^- in the Q valley, which results in a virtual energetic state in K, energetically lowered by the phonon energy. Due to zero wave-vector difference, the exciton radiatively recombines. Symmetrywise, the same process occurs for the K' and Q' valley. Interestingly, $k(K - Q) \sim k(Q)$, such that phonons from the Q-point meet the above mentioned condition.

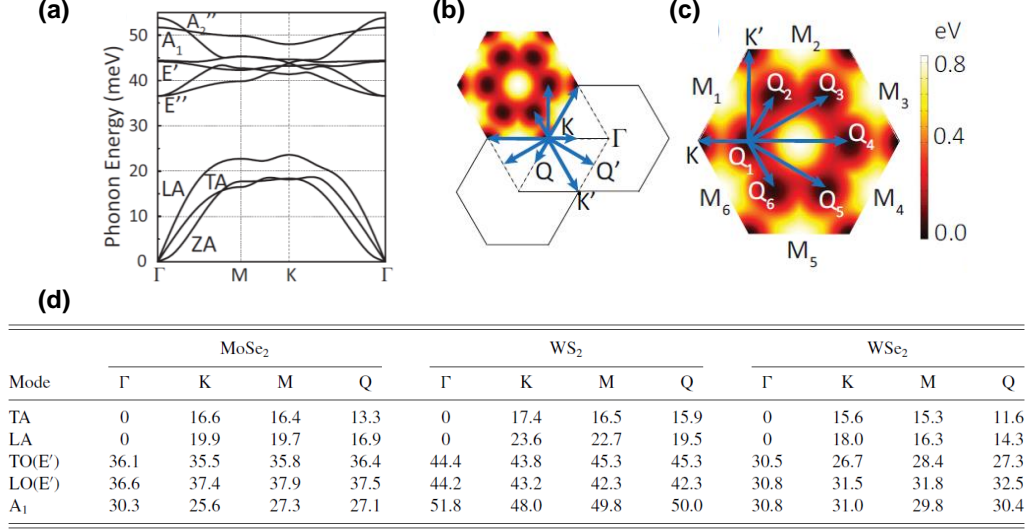


Figure 2.5: **(a)** Phonon dispersion relation of the first Brillouin zone for the exemplary case of WS₂, with similar behaviour for all TMDs. Corresponding phonon energies for all momenta can be extracted and used in further calculations. Schematic illustrations of inter-valley scattering processes for electrons in the K valley **(b)** and in the Q valley **(c)** of WS₂. The vertical colour bar represents the electron energy with respect to zero at the bottom of the CB. **(d)** Table of phonon energies at high symmetry points of the reciprocal lattice. Graphics taken from [20]

Taking the full first Brillouin zone with all possible electron scattering processes into account, we introduce a phonon sideband model [2] which aims to reproduce observed photoluminescence (PL) spectra for tungsten based TMDs.

The two energetically lowest conduction bands and the highest valence band are taken to account for possible exciton formations. The h^+ is fixed to the upper valence sub-band at the K-point. Six states are considered in the CB: The spin- and momentum direct state, formed by the e^- in the upper branch at the K point and the h^+ at the CB in K, labeled as "bright" (B) and commonly referred to as A-exciton. It has the character of circular, out of plane emission and due to parallel spins, a total projection of $|m_s\rangle = |m_{s_{e^-}} + m_{s_{h^+}}\rangle = +1$. The dark state (D), introduced in section 2.2, has $|m_s\rangle = 0$ due to anti-parallel spins of e^- and h^+ and therefore is referred to as "spin-dark". As both the B and the D-states are momentum direct, no phonon is needed for a radiative recombination. The next states are the spin-bright Q and spin dark Q' valleys, both momentum-dark. At last, e^- from the spin-dark and spin-bright K' valleys are considered, which can

become momentum direct via a second order process involving a phonon with momentum k . A schematic depiction is presented in figure 2.6.

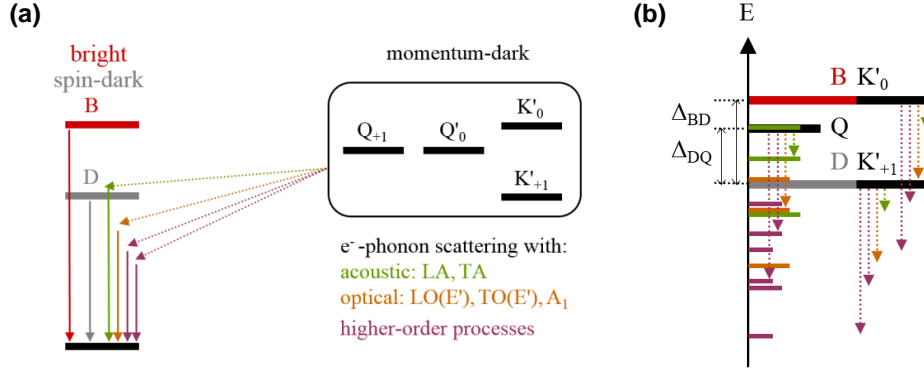


Figure 2.6: **(a)** The six valleys in the lowest two CBs are grouped into momentum-bright and dark states. The spin-bright and spin-dark states are displayed in red and grey, with direct radiative recombination marked by arrows. The momentum dark states can become momentum direct with a second order process, involving a phonon. Acoustic and optical phonon-processes are marked in green and orange respectively. Higher order processes involving multiple phonons from the Γ point can lead to energetically lower-lying virtual states. **(b)** Energetic ordering of the contributing CB valleys, where coloured bars are phonon replicas. Only the stokes side of the scattering process is taken into account. Therefore the model is referring to cryogenic temperatures. [2]

The six CB states are grouped into momentum bright and dark, whereas the subscripted index displays the total spin projection. The radiative decay channels of the momentum direct B- and D-states are indicated by red and grey arrows. Momentum-dark (indirect) states can only decay radiatively with the assistance of acoustic, optical, or higher-order phonon processes, indicated by green, orange and purple arrows respectively. The latter occurs with additional Γ -phonons of zero net momentum but finite energy contributions to the scattering process. A schematic decomposition of the PL-spectrum is shown in 2.6 (b). The same color code as in (a) is used and resulting phonon replicas are energetically ordered. Only the stokes-side of the scattering process is taken into account, leading to an energy reduction of the corresponding state by the phonon energy. Anti-stokes processes may occur at room temperatures, but for the typical, cryogenic temperature of 4 K they are negligible due to the small population of phonon states. Corresponding exciton energy splittings are labelled Δ_{BD} , the

energy difference between the B- and D states. Δ_{DQ} denotes the energy difference between the Q- and D states.

The broken inversion symmetry allows an implementation of exciton formations with the hole at K'. However, this is neglected in the following. For spectral decomposition processes, this would not change the fundamental predictions made by this model. The upper sub-bands at Q and Q' in the CB are disregarded due to their large spin-orbit splitting of $\sim 100\text{meV}$ [22].

Sample fabrication and characterization

This chapter reports on the methods used for sample fabrication and characterization. Hereby heterostructures consisting of transition metal dichalcogenide monolayers (TMD-MLs) and hexagonal boron nitride (hBN) were built and examined. The identification of monolayer TMDs on a given substrate is thereby an essential component.

3.1 Mechanical methods

3.1.1 Exfoliation of two dimensional crystals

A variety of single- and few-layer two dimensional materials can be prepared either by a bottom-up approach via chemical vapor deposition (CVD) [13], or by the top-down method of micro-mechanical exfoliation[16]. The latter is often referred to as the "Scotch tape method". In combination with deterministic transfer methods discussed in 3.1.3, it allows a rather simple approach for assembling van der Waals (vdW) heterostructures [12].

The inter-layer vdW bonds in bulk TMD crystals are cleaved down to the monolayer limit by repetitive use of adhesive tape. A stripe of Nitto Tape BT-150P-LC is brought into contact with bulk material provided by HQ Graphene (Figure 3.1(a)) and removed such that a small piece of bulk adheres to the tape. The tape is matched with a second tape and pressure is applied to ensure contact, reduce air blisters and thereby maximize the adhesive forces between the tape and the crystal. Next, the tapes are pulled apart and the procedure is repeated three to four times with one of the tapes. A sizeable area is then covered with flakes (figure 3.1(b)), where the expression flake refers to separate regions of 2D crystals in various forms and thicknesses.

Now the tape is brought into contact with the desired substrate, pressure is ap-

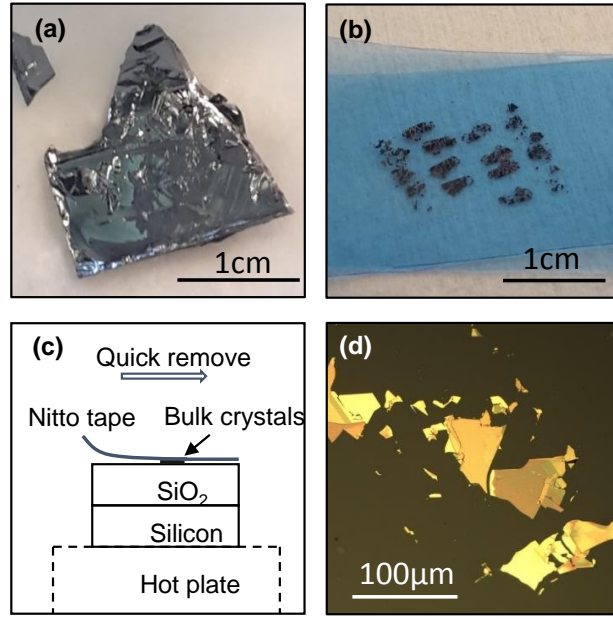


Figure 3.1: **(a)** Bulk crystal of MoS₂. **(b)** Nitto tape after exfoliation from bulk and repetitively exfoliation to a sizable area covered with crystal layers. **(c)** Schematic illustration of the final exfoliation step. Contact of the SiO₂/Si substrate with the prepared tape and subsequent quick remove is leading to direct exfoliation of layered crystals onto the substrate. Indicated hot plate can be used for 2 minutes at 100°C to increase the adhesive forces between the two interfaces, leading to a higher yield of exfoliated and transferred flakes but induces also tape residues over the surface. **(d)** Optical microscope image of Mo₂ crystals on top of SiO₂/Si. Edges break in a multiple of 60° due to the hexagonal lattice structure, resulting in a variety of visible formations.

plied and subsequently the tape is quickly removed (see 3.1 c). Flakes are randomly exfoliated on the substrate. The sizes and heights of these flakes vary strongly. An optical reflection microscope (Olympus® - BH2-UMA) image of such flakes on a silicon wafer covered with a 90nm SiO₂ is shown in figure 3.1 (d). Mono- and few-layer flakes are searched with the analysis of optical contrast between the flake and the substrate. More details are shown in section 3.3.3.

It is important to point out that monolayer and few layer flakes are cleaved from the multi-layer crystal and not from the tape itself. The actual exfoliation step is governed by competition of vdW-forces between the two different interfaces. The interface between the outermost layer and the substrate competes with the vdW forces inside the crystal [19]. By quick removal of the crystal-covered tape from the substrate, the bonds between the substrate and the outermost layer partly overcome the inter-layer bonds. This randomly produces flakes with a wide range of sizes leading to single-layer terraces as well larger steps in thickness. Atomic force microscopy was used to further characterize the flakes, where it was found that the edges are markedly higher than the rest of the flake. The forces exerted during the exfoliation process are inhomogeneous, which especially affects the less bound outermost hexagonal unit cells. Therefore, more layers are transferred in the border region of a flake, whereas the central region can still be in the monolayer limit.

Di-oxygen (O₂) plasma pre-treatment of the substrate as well as thermal release of adhesive tape have been established as techniques to increase the yield of exfoliated monolayers [19]. O₂ plasma cleaning removes adsorbates from the SiO₂ / Si substrate. In this work, SiO₂ / Si substrates were plasma cleaned for 30s in a commercial machine (Gigaetch 3000) with a power of 200 W. The tape is brought into contact with the substrate directly after the plasma treatment which increases the adhesive forces between the substrate and the flake. The substrate, whilst in contact with the tape, can additionally be placed on a hot plate at 100°C for 2 minutes. Residual trapped water molecules and other adsorbates evaporate to the sides of the flake, reducing the layer-substrate spacing, which in turn enhances the vdW interactions at the interface. The tape is removed after cooling to room temperature. Water trapped between the interfaces causes height variation of monolayer TMDs in AFM measurements. The heights measured are typically ≈ 0.9 nm- roughly three times higher than the theoretical crystal height of 0.31 nm for MoS₂ [39].

Both methods lead to an increase in the number and size of exfoliated layers. However, they can impact the device performance. Annealing the sample with tape in contact increases the amount of tape residues left on the sample. Additionally, the pressure built up by evaporating water can partially break the flake

and induce strain. Further discussion can be found in chapter 3.4.2. O_2 plasma is known to introduce trapped charges in oxidized silicon. The modified doping level of the substrate can later on affect confocal cryogenic measurements [29].

3.1.2 Hexagonal boron nitride

Similarly to the depicted transition metal dichalcogenides, boron nitride also adopts a hexagonal form (hBN), where atomic layers are coupled via vdW forces to a bulk crystal. It is an indirect bandgap semiconductor, optically active in the ultraviolet and shows varying crystal qualities in recent synthesis techniques [3, 10]. Despite its optical properties, its surface is extremely flat, homogeneous and electrically calm.

Dangling bonds on the silicon surface can locally and temporally bind charges and thereby induce charge fluctuation in the substrate. To exclude these charge effects, hBN was recently investigated by a variety of groups working on two dimensional materials, where surface effects play a dominant role. All underlying physical processes and energy transitions can only be addressed experimentally, when an inhomogeneous broadening by environmental perturbations is minimized to the limit of modern technology. Not only is hBN used as a substrate, but also as a capping layer which additionally screens the layered crystal from the environment and shows intrinsic life-time broadened spectral widths at cryogenic temperatures. [1, 7, 37]

Thus hBN became the preferred dielectric substrate for monolayer TMDs in this work. First, commercial hBN bulk crystals from HQ graphene were exfoliated with Nitto tape onto a SiO_2/Si wafer in the same way as TMDs. The typical bulk crystal depicted in the inset of figure 3.2 (a) has a diameter of ≈ 1 mm, which is small compared to the bulk crystal of TMDs with a size of above 1cm. The yield obtained from direct exfoliation was therefore initially smaller, making the in chapter 3.1.1 mentioned methods of thermal annealing and plasma treatment necessary.

Shown in figure 3.2 (a) is an optical microscope image of exfoliated hBN on SiO_2/Si . Varying height results in a periodical change of the dominant reflection wavelength. Figure 3.2 (b) depicts typical border regions of an exemplary hBN flake. Terraces are depicted and mapped to certain heights via atomic force microscopy, seen in figure 3.2 (c) and (d). The c-axis lattice constant of a hBN monolayer is calculated to be 0.33 nm [18]. AFM measurements show a height of ≈ 600 nm for the exemplary flake, approximately 1800 stacked single layers. Even though hBN is transparent, the Bragg condition $2d\sin\theta = n\lambda$ holds for

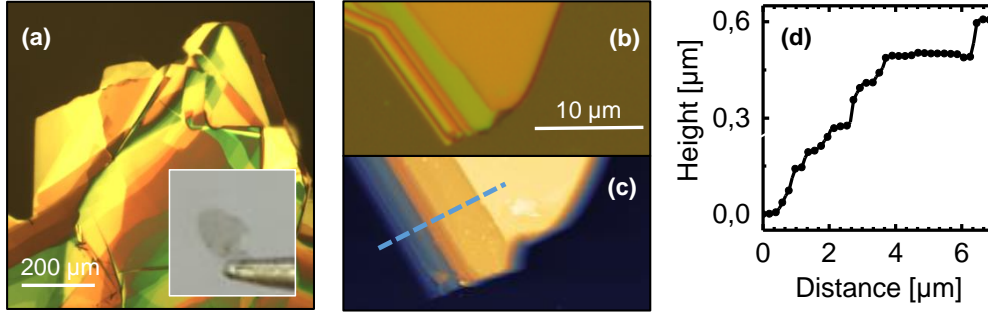


Figure 3.2: **(a)** Optical microscope image of exfoliated hBN on a SiO₂/Si wafer. Inset: typical bulk crystal approximately 1mm in diameter. **(b)** Extended picture of a flake with terraces at the border. Inset shows the sample with the scalebar of 500 μm. The dashed line indicates the region investigated under AFM in **(c)**. By mapping the AFM values for height **(d)** to the optical contrast a rough estimation of the height can be deduced.

the partially reflected light, which leads to color variation via constructive interference. In this work, hBN flakes were examined under constant illumination conditions and by cross linking the optical contrast with an AFM data set, their thickness could be roughly determined. Additional ellipsometry measurements can be used to further specify the height.

3.1.3 Transfer by viscoelastic stamping

A deterministic transfer technique is implemented in order to transfer monolayers of TMDs onto hBN exfoliated on SiO₂/Si substrates. The dry transfer of 2D materials via visco-elastic stamping was first shown by Castellanos-Gomez [12] and a schematic setup is depicted in figure 3.3.

A transparent glass slide is prepared with a film of polydimethylsiloxane (PDMS) (Gel-Film® PF-X4-6mm) and layered crystals are exfoliated onto the PDMS. Afterwards, the stamp is examined under an optical microscope and monolayer regions are marked (exemplary depiction of a monolayer in figure 3.4 (b)). The stamp is then placed onto the stamping stage, with the flakes facing the substrate. The substrate is fixed to the sample stage by double sided tape.

The Setup implements two horizontal planes of movement where either the substrate or the objective can be positioned by mechanical controllers. The transfer process is depicted schematically in figure 3.4 (a). First, the target substrate was

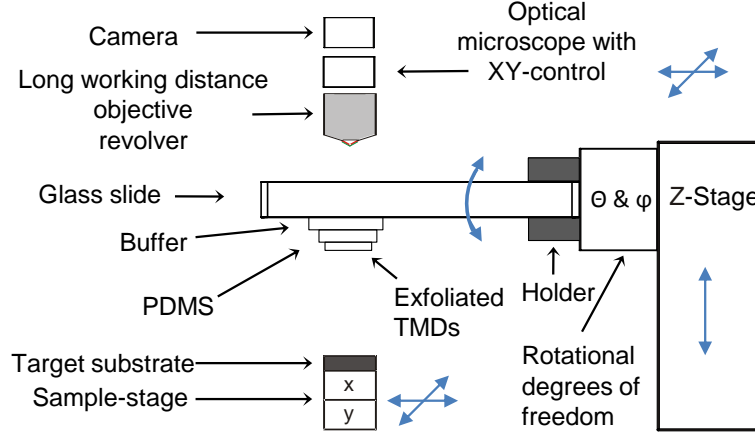


Figure 3.3: Schematic representation of the setup used for transfer. Blue arrows indicate translation and rotational degrees of freedom used for alignment of the stamp with the substrate.

aligned to the monolayer marked on the stamp. The focal plane was thereby repeatedly switched between the monolayer and the substrate while lowering the stamp. Before contact, the rotational degrees of freedom implemented on the glass-slide holder were used for parallel alignment of the interfaces. Final corrections to the horizontal position of the substrate were made, followed by slow lowering of the stamp. After first contact of the interfaces, the rotational axes were used to "roll over" the substrate and the z-position was carefully adjusted to ensure contact. The border between in and out of contact interface regions is clearly visible in the objective, depicted in figure 3.4 (c). Upon full contact, the stamp is slowly removed and the transfer process is completed by subsequent annealing. An exemplary microscope image after successful transfer is shown in figure 3.4 (d).

The mechanical control of this interface is a crucial factor. The vdW forces between the monolayer and the hBN flake must exceed the bond strength between the PDMS and the monolayer. Slow contact ensures homogeneous binding and increases the transfer rate. Besides, the more the movement of the contact border over the target surface is controlled, the less strain is applied to the monolayers. Strain effects on monolayers influence the crystal quality and systematically shift the bandgap [49]. It is therefore crucial to control this parameter when mapping optical signatures to physical properties. The transfer method of viscoelastic stamping, however, does not exclude induced strain effects on the crystal.

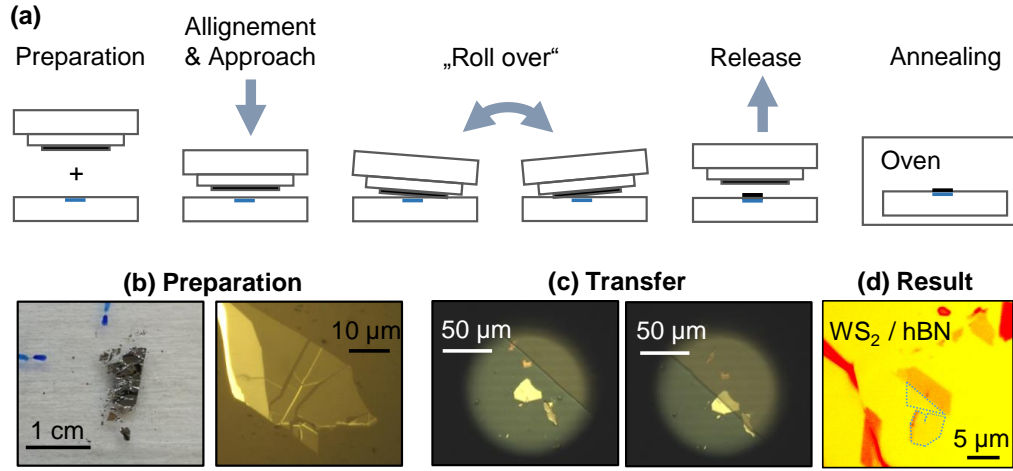


Figure 3.4: **(a)** Schematic representation of the transfer process. **(b)** Optical microscope picture of transparent PDMS on a glass slide, with exfoliated WS₂ on top. The blue lines mark the position of the monolayer, displayed in **(c)**. Figures **(d)** and **(e)** show an exemplary transfer process at two different time steps. The edge displays the border region of contact. **(f)** Modified optical image of a resulting heterostructure, where the dashed lines mark the ML position on top of hBN.

It is useful to implement a buffering layer between the glass slide and the PDMS to reduce both, the impact of misalignment of the setup and pressure between the interfaces. The buffering material can either be another uncovered PDMS slide or any transparent double sided tape, as long as the binding forces exceed the adhesive forces between the stamp and the substrate.

3.2 Optical setup

Optical measurements were carried out using either a confocal microscope setup or an imaging setup, implemented by Andre Neumann [27]. The setup is operated at room temperature or placed inside a liquid helium can at 4 K.

In confocal microscopy, light is focused to a diffraction limited spot size of $\approx 1 \mu\text{m}$ via a low temperature apochromat. The signal is detected at the same spot and spectral information is collected by a spectrometer with a liquid nitrogen-cooled charge coupled device (CCD). This configuration is used for photoluminescence (PL)- and Raman-measurements as it allows spectral analysis. In contrast, the PL-imaging configuration illuminates a wide field diameter of $\approx 50 \mu\text{m}$. The col-

limation of the laser beam is set such that the full diameter of the objective is illuminated. The sample is placed in the focal plane whereas the excitation is not. The resulting PL is mapped onto the CCD chip of a camera (Point Grey® Grasshopper 3), where spectral information is collected via selected filter settings. A schematic of both setups is shown in figure 3.5.

For excitation, the following lasers were available: A super continuum white light laser from NKT for pulsed excitation with various wavelengths and continuous wave (cw) diode lasers at wavelengths of 532 nm and 632 nm. A single mode optical fibre guides the laser to the excitation arm. Polarization panels determine a polarization inside the fibre. An optical collimator expands the beam and a linear polarizer defines the excitational polarization axis. The raman signal from the fibre is filtered by short-pass filters, blocking transmission above the laser wavelength. The beam is partly reflected at a broadband beamsplitter. The transmitted light is detected with a photo-diode, which was used for adjustment purposes. The beam is focused onto the sample with a custom-built low temperature apochromat with a numerical aperture (NA) of 0.65. The sample was placed on top of slip-stick piezo nanopositioners with resistive readout, operated in stepping mode for single point measurements. The reflected and emitted light was collected by the same objective and transmitted through two beam-splitters, where a marginal part was guided towards a reflection camera used for positioning and focus-control. The signal (indicated by red lines in figure 3.5) is then separated from reflective light by suitable long- or bandpass-filters. For cryogenic measurements, the part indicated by the dashed blue line was placed inside a tube, shielding the sample from the surrounding liquid helium. Helium exchange gas ensures thermalization of the sample. In confocal configuration, the light is then coupled into a fibre by an apochromatic lens which guides the signal to a grating-spectrometer. In imaging configuration a Galileo telescope consisting of a bi-convex and plan-concave lens is placed in front of the CCD chip of a USB camera. The camera settings are controlled by a PC.

3.3 Layernumber quantification

This section will give an overview of the different methods used for layernumber quantification. As the unit cell of TMD-crystal has a height of approximately 0.3 nm, detecting differences in layernumber on a single-layer scale was initially challenging. One method is Raman spectroscopy. The layer dependent vibrational modes found for all TMDs examined in this work, enabled the identification of mono- bi- and trilayers exfoliated on a silicon substrate. The PL-imaging

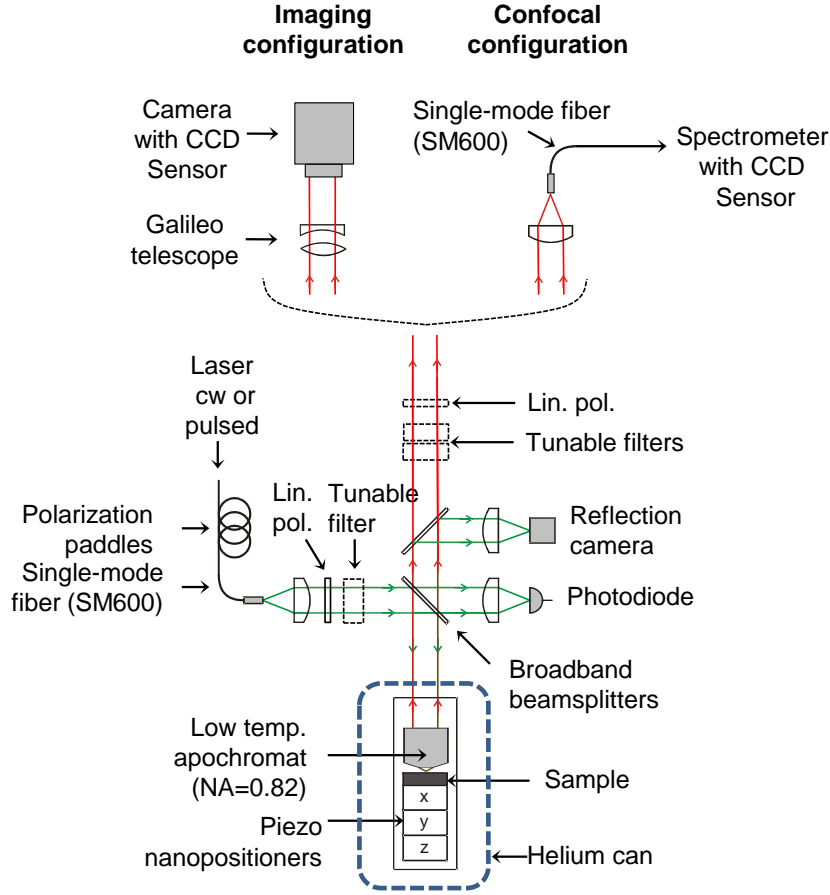


Figure 3.5: Setup used for confocal measurements and PL-imaging. The excitation laser is guided with a single-mode fibre towards polarization optics. Implemented optical filters exclude higher order modes and broadband beam splitters reflect the beam towards the sample placed on piezo nanopositioners. In the confocal configuration, the beam is collimated and focused directly onto the sample by the apochromat. The PL signal, together with reflected light, is collected from the same focal spot and transmitted through two beam splitters and optical filters, isolating the signal from reflective laser light. After coupling to a fibre, it is analyzed in a grating spectrometer with a cooled CCD sensor. The imaging configuration differs in collimation, where the beam is aligned, such that the full objective is illuminated and therefore the excitation is out of focus. The signal is not coupled into a fibre, but directed via a galileo telescope onto the CCD sensor of a USB camera. The dashed blue line indicates the part of the setup, which is placed inside a tube filled with helium exchange gas and inserted into a helium can, when measuring at cryogenic temperatures.

setup described above not only identified the few-layer thicknesses of flakes on stamp by intensity, but also allowed for quality characterization. Finally, optical contrast analysis of flake-images from a reflection microscope is shown. With fixed illumination conditions and confirmed layer-thickness from two other approaches, optical contrast is a reproducible and quick method to identify the layer-number.

3.3.1 Raman spectroscopy

In Raman spectroscopy, inelastic scattering of light allows the excitation of well defined vibrational and rotational modes of a given material. It has proven to be a powerful tool in determining the exact number of layers of exfoliated MoS₂, MoSe₂, WS₂ and WSe₂ [33, 45, 46].

Group theoretical analysis of the D_{6h} group predicts four active raman modes; three in-plane modes E_{1g}, E_{2g}¹ and E_{2g}², as well as one out-of-plane mode A_{1g}, schematically shown in figure 3.6 (a). The E_{2g}¹ and A_{1g} modes are easily accessible and show a strong shift in frequency depending on the exact layer number. For MoS₂ and WS₂, the frequency difference between these modes increases with layer number. The value for a MoS₂ monolayer on SiO₂ is $\Delta f = 19 \text{ cm}^{-1}$, and $\Delta f = 21 \text{ cm}^{-1}$ for a bilayer [23, 41]. WS₂ shifts from $\Delta f = 60,5 \text{ cm}^{-1}$ to $\Delta f = 62,5 \text{ cm}^{-1}$, where for unpolarized excitation the E_{2g}¹ is overlapped by a second order raman mode due to LA phonons at the M point of the Brillouin zone, denoted as 2LA(M) [45, 46]. For MoSe₂, the E_{2g}¹ is weak and the out-of-plane A_{1g} mode changes in position and intensity with increasing layer number. Peak positions in the mono- and bilayer cases are compared to [33]. WSe₂ shows no separation between E_{2g}¹ and A_{1g} peaks. The main feature in this case is the 2LA(M) mode centered around 250 cm^{-1} . The peak located at around 308 cm^{-1} is possibly a combination of a shear mode with the E_{2g}¹ mode, and is absent in monolayers [46]. An overview of peak positions from literature is shown in figure 3.6 (b).

Raman modes of MoS₂ on a silicon substrate were measured at room temperature in confocal configuration with a laser-notch filter and a linear polarizer in the excitation arm and no longpass filter in the detection arm. The grating of the spectrometer was chosen such that laser emission at 532 nm for MoS₂ was not captured by the CCD, as this could permanently impair sensitivity. Measurements on MoSe₂, WS₂ and WSe₂ were made at 514 nm excitation with a commercial Raman-setup, provided by the Group of Prof. Feldmann. Results are shown in figure 3.8.

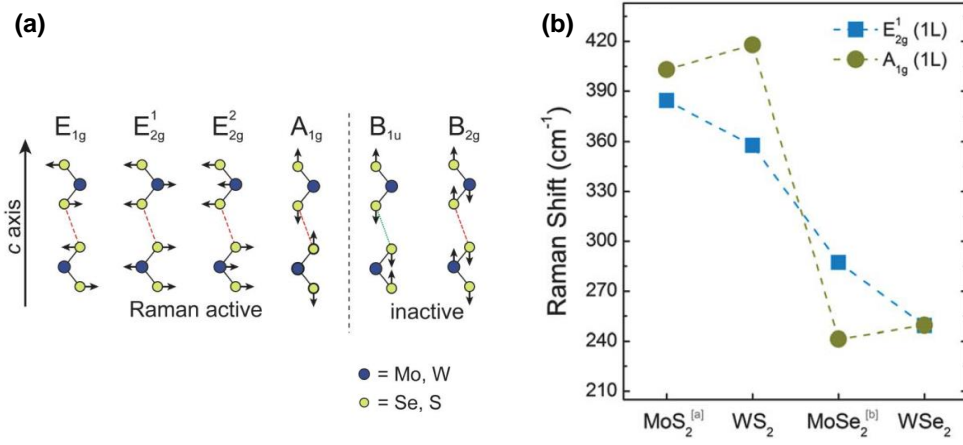


Figure 3.6: **(a)** Four active raman modes and two inactive modes are schematically depicted. Blue dots represent transition metal atoms, molybdenum and tungsten respectively, where the yellow dots are the chalcogen atoms sulfur or selenium. Arrows indicate the vibrational axis of the atoms. **(b)** Raman shift of the E_{2g}^1 and A_{1g} modes for monolayer of MoS₂, MoSe₂, WS₂ and WSe₂. The layernumber can be determined via the separation of these two modes. WSe₂ shows no separation between the E_{2g}^1 and A_{1g} peaks and the layernumber is determined by the absence of a side peak around 308 cm^{-1} . Graphics taken from [33, 46].

3.3.2 Photoluminescence-imaging

The imaging configuration of the optical setup shown in 3.2 is the second approach to determine the layernumber. As TMD monolayers have a direct bandgap, the radiative relaxation channels are more profound, and compared to the bilayer or trilayer cases, the resulting PL signal is much higher. In this work, the most prominent TMDs: MoS₂, MoSe₂, WS₂ and WSe₂, were investigated on stamp at room temperature. Suitable short- and long-pass filters are chosen, such that the reflected laser light is completely blocked. Raman modes from the fibre are suppressed and the full PL signal is detected. Additionally, a linear polarizer is set to cross-polarization configuration so as to block residual reflected laser light. A spectral overview of the investigated materials obtained by this group is shown in figure 3.7, where the energetic peak positions stay in good agreement with literature values [9, 33, 43].

The camera of the imaging configuration was controlled using a PC with the software LABVIEW. The parameters are: integration time, gain and gamma. The

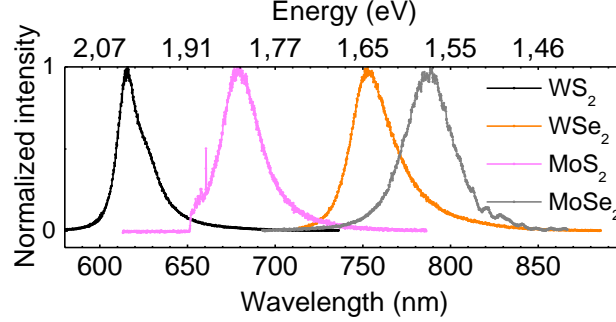


Figure 3.7: Room temperature PL-spectra of MoS₂, MoSe₂, WS₂ and WSe₂ from this group. The intensity is normalized to 1. The emission wavelengths cover a range of 600 nm to 850 nm. The data is in good agreement with literature [9, 33, 43] and is used to set filter settings for PL-imaging.

raw signal comes from photons originating in recombination processes inside the 2D crystals. They encounter an array of photo diodes, the CCD sensor of the camera, which converts the number of incident photons in a certain time interval to a number of electrons via an intrinsic photoeffect. With an analog to digital converter (ADC), each pixel is assigned to an intensity $I = E \cdot ADC$, where $ADC = (pixel\ capacity)/(2^{Bit})$. *Bit* refers to the image format chosen. I is the digital output and E the number of electrons. The variable gain, G , can be implemented to magnify I in following way: $I_g = I \cdot 10^{(G/20)}$. At last, gamma (γ) is applied, giving in 16-Bit format:

$$Pixel\ value = (2^{16} - 1) \cdot (I_g/2^{16})^{(1/\gamma)}$$

In figure 3.8, an overview of the identification process is shown. The four most prominent TMDs were exfoliated on a PDMS stamp. Pictures were taken with the illumination conditions outlined in chapter 3.3.3. PL-imaging was carried out to confirm layer thickness. For MoS₂, a different objective was used than for the other materials. Therefore the intensity is not directly comparable to that of the other materials. For MoSe₂, WS₂ and WSe₂, mono- and bilayers are visible in photoluminescence, where the darker region indicates a bilayer. For WSe₂, even a trilayer is visible when integrated over 30s, shown in the inset. For all pictures shown here, Gain was set to 24 and Gamma to 0. The integration time is indicated inside the pictures. For excitation, the super continuum white light laser source (WLS) was set to an emission wavelength of 520 nm to 560 nm, with a repetition rate of 78 MHz. These settings resulted in an excitation power of 350 μ W, corresponding to 17.8 W/cm^2 for an illumination radius of 25 μ m.

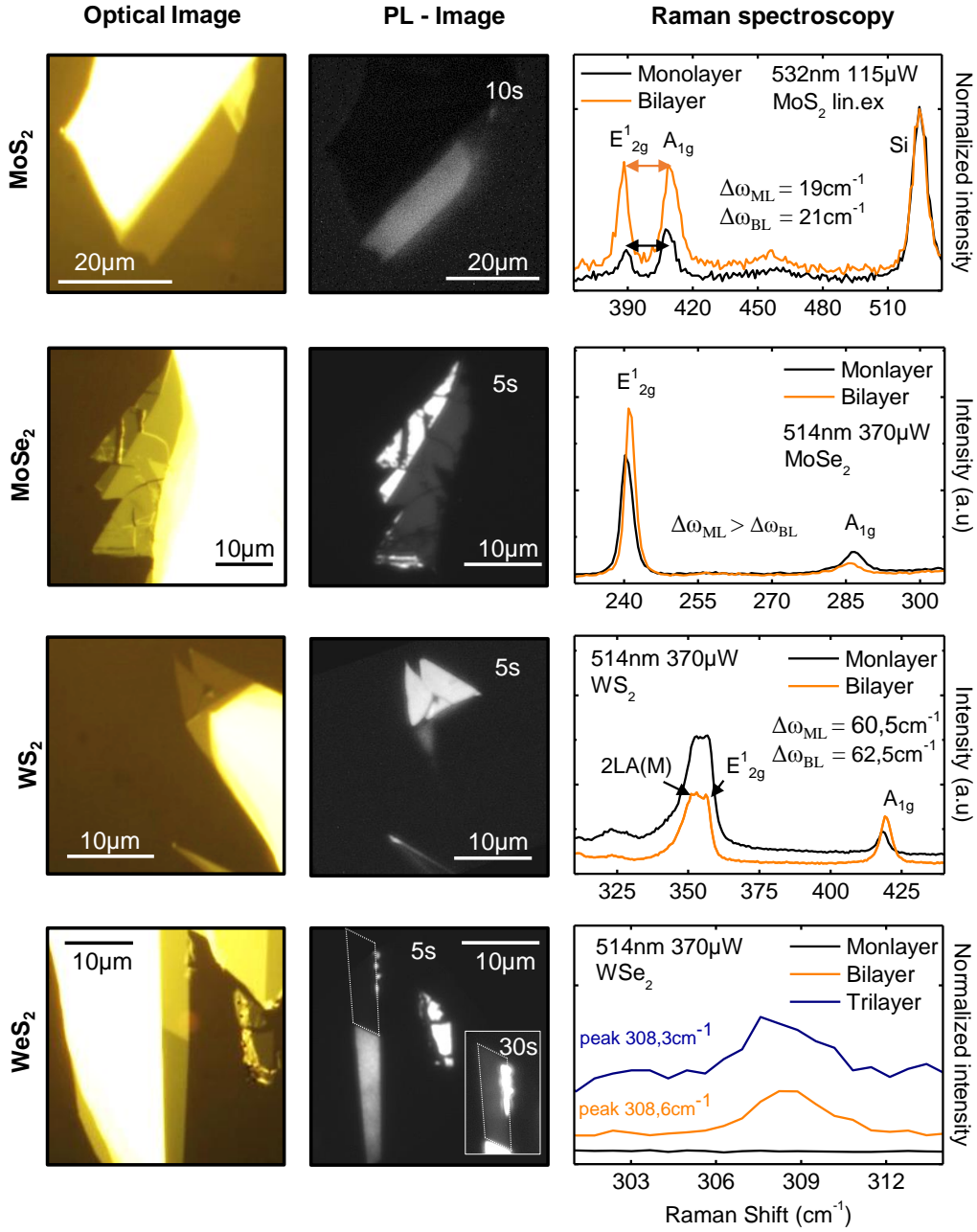


Figure 3.8: **Left panel:** Optical images of flakes on PDMS with equal camera settings. A slight variation in contrast is noticeable. **Middle panel:** PL-images identify monolayers as well as bilayers for MoSe₂, WS₂ and WSe₂. All images except MoS₂ were made at identical experimental settings. Integration time is indicated. Even a trilayer is revealed for WSe₂, shown in the inset. **Right panel:** Raman spectra to confirm the results. For MoS₂, MoSe₂ and WS₂, the E_{2g}¹ and A_{1g} modes are displayed. By their separation, the layernumber can be determined exactly. For WSe₂, a sidepeak disappears in the monolayer limit.

The advantage of PL-imaging is the direct extraction of the layernumber from flakes on the PDMS stamp, whilst Raman spectroscopy was carried out after transfer onto SiO₂ / Si substrates. Additionally, the spatial information of the photoluminescence allows a first quality characterization of the few-layer flakes, further discussed in chapter 3.4.

3.3.3 Optical contrast

The two complementary methods of layernumber characterization described above now allow the analysis of optical contrast from pictures taken with a camera positioned on top of the reflection microscope (Olympus® - BH2-UMA). This approach is very sensitive to illumination conditions as well as camera settings and was therefore initially carried out on flakes with confirmed layer thickness by Raman spectroscopy and PL-imaging. Illumination was provided by a halogen lamp with manual brightness control via a potentiometer. The contrast between the flake and the substrate strongly depends on the number of crystal layers [11]. Fixed illumination conditions and camera settings, seen in table 3.1, gave comparable pictures and reproducible results.

Camera parameter	Values
Gain	226,3
Gamma	2,04
Colour balance	neutral
Yellow filter	used
Illumination	8

Table 3.1: Camera settings for the Olympus® microscope in the clean-room

With the image post-processing software ImageJ, further analytical steps were carried out. First, the RGB-picture of the camera, shown in figure 3.9 (a), was split into three separate grey scale images, each representing a colour channel. A significant difference in grey scale intensity between a mono and bilayer was found in the red channel. This is not surprising, as the optical response of the TMD-ML examined in this work is found to be in the red visible regime as seen in figure 3.7. Regions with percentage threshold values of 6% to 9% for the monolayer and 12% to 20% for the bilayer are marked in red in figures 3.9 (b) and (c). Differences between MoS₂, MoSe₂, WS₂ and WSe₂ in the resulting optical images fit inside these threshold values. Care has to be taken on the inhomogeneous illumination of the microscope which leads to position-dependent results. Therefore, the flake of interest was always centered in the scope of the camera.

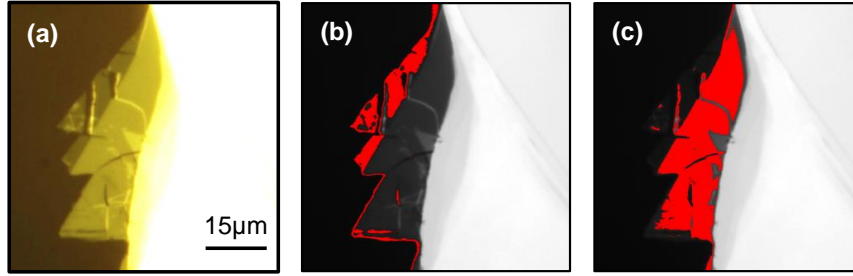


Figure 3.9: **(a)** Optical microscope picture of mono- and bilayer MoSe_2 next to bulk crystal. Illumination conditions are fixed (see table 3.1). Scale bar $10\mu\text{m}$. Wrinkles in the border regions and within the flake are visible by varying contrast in these regions. **(b)** Grey scale image was filtered for values between 6% and 9% of maximal pixel value in the red channel. These pixels are displayed in red and match the monolayer confirmed by Raman spectroscopy 3.3.1 as well as PL-imaging 3.3.2. Figure **(c)** displays threshold values of 12% - 20% and identifies the bilayer.

3.4 Sample characterization with photoluminescence-imaging

The PL-imaging approach allows not only few-layer identification due to the resulting pixel intensity by fixed setup parameters, but also gives a quick insight to the lateral luminescence distribution of the sample. This gives information on the sample quality. It was found that residues and sample disorder are displayed in the spatial PL distribution. As the size of exfoliated few-layer TMD crystals in this work does not exceed the illumination diameter of approximately $50\mu\text{m}$, the flake is fully captured in a single picture .

3.4.1 Silver substrates

It was shown that coupling TMD monolayers to a micro-cavity enhanced the light-matter interaction in such a way that new physical phenomena arise as the strong coupling regime is reached [25]. In this context, experimental efforts were made to build a planar cavity out of two sputtered silver (Ag) layers with SiO_2 as a spacer material and a monolayer of MoS_2 in the center. As the samples were unfortunately destroyed in the process of fabricating the topping layers, this work will only show first results of a monolayer on a SiO_2 / Ag substrate.

Monolayers of MoS₂ were transferred onto a self-designed mirror. Hereby, a SiO₂ / Si wafer was sputtered with a 200nm-230nm thick silver layer. To exclude quenching effects from the silver substrate on the photoluminescence of the ML and in order to position the ML away from the node of the reflected light, 90 nm SiO₂ was sputtered on top, which also prevented oxidation effects on the silver. A direct comparison of the PL-images from a MoS₂ ML on a SiO₂ / Si wafer and the silver substrate described above is shown in figure 3.10.

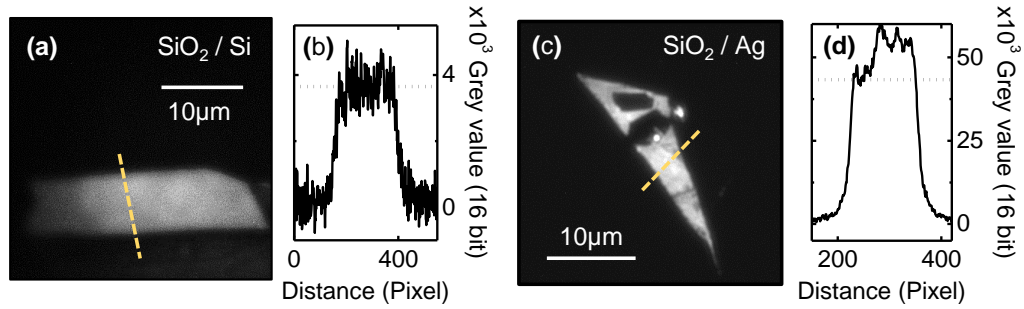


Figure 3.10: **(a)** Brightness enhanced PL-image of a MoS₂ monolayer on SiO₂ / Si. The yellow dashed line indicates the initial pixel read out shown in **(b)**. The grey value increases by ≈ 4000 when read out over the flake position. **(c)** PL-image of a MoS₂ monolayer transferred onto a SiO₂ / Ag / SiO₂ / Si substrate with pixel readout displayed in **(d)**. A comparison of the pixel intensities from the two MLs at equal experimental conditions reveals a magnification on the silver substrate by a factor of ≈ 11 .

The PL-images (a) and (c) were integrated over 5 s in cross-polarization configuration, with the settings described in chapter 3.3.2. The brightness in figure 3.10 (a) is modified for clarity. Pixel values along the dashed blue lines are displayed in (b) and (d). The ML on SiO₂ / Ag shows ≈ 11 times the intensity of the ML on the SiO₂ / Si substrate, with very different signal to noise ratios (40:1 and 4:1, respectively). The image sharpness of the monolayer on silicon is worse than on silver. This indicates an experimental misalignment, thus a strong error for the enhancement factor.

The vertical reflectance at $\lambda = 680\text{nm}$ is 0,991 for Ag and 0,341 for Si. The dipole emission of the excitonic PL is mainly directed towards the sample due to the dielectric environment. Enhancing cavity effects between the Ag-interfaces additionally occur, leading to an overall amplification of the signal.

Inhomogenities are noticeable in the PL image 3.10 (d). Two bright dots appear, as well as a brighter region in the center. The blue dashed line indicates exemplary chosen pixel values displayed in (f). The dots are most probably small parts of

flakes where strain effects and quantum dots, arising in the fabrication process, dominate. Despite the intrinsic band structure of TMDs, such perturbations can open up localized relaxation channels and thereby increase the total amount of integrated intensity. The step-like increase of the pixel values along the blue line can have multiple causes: residuals between the flake and the substrates e.g. water molecules accumulate to defined regions, PDMS from the flakes partially covers the surface, or a wrinkle of the flake locally suspends the flake from the surface, leading to an intensity increase due to the change of the effective local dielectric environment. For the latter, no such wrinkle appears in the optical microscope picture, therefore residues are the most plausible explanation.

3.4.2 Annealing

To exclude water molecules in the flake-substrate interface, thermal annealing showed promising results [37, 38]. An annealing oven with an implemented high vacuum chamber was used in this work. The samples were annealed for two hours at a temperature of 400°C. Trapped water is evaporated, reducing the distance between flake and substrate. The pressure built up between the interfaces smoothens the flake surface and reduce wrinkles, but can also break the flake and partially detach it. To minimize such effects, the temperature was risen up with not more than 1 °C/s. Especially around the boiling point of water, slow increase of temperature as well as thermalization was ensured.

In figure 3.11, a MoSe₂ / hBN heterostructure on SiO₂ / Si is shown in PL-imaging at room temperature before annealing (a), after annealing (b) as well as after encapsulation with a hBN-topping and repeated annealing (c). The flake quality after the transfer process is very poor. The lower left part is darker than the rest, many dots of unequal intensity are visible and a wrinkle from the top to the center right side of the flake appears. Homogeneity after annealing increased drastically. The wrinkle smoothed out, the dots essentially disappeared and the intensity in the bottom left corner matched that of the remaining flake. A crack appeared, a side effect of the annealing protocol. Even so, some darker regions are identified - the sample is still not uniform. Encapsulation involves a second transfer process and thus, a second critical step where strain effects appear. Residual molecules are trapped between the flake and the capping layer of hBN. Even after annealing, these additional impurities did not disappear, demonstrating the limit of this technique. The underlying mechanical effects, which are not controlled on a nano-meter scale, also cause stochastic variance. Interestingly, the most unperturbed spectrum at 4K was emitted in the relatively dark region in (c), indicated by the yellow dashed circle and further discussed in chapter 5.

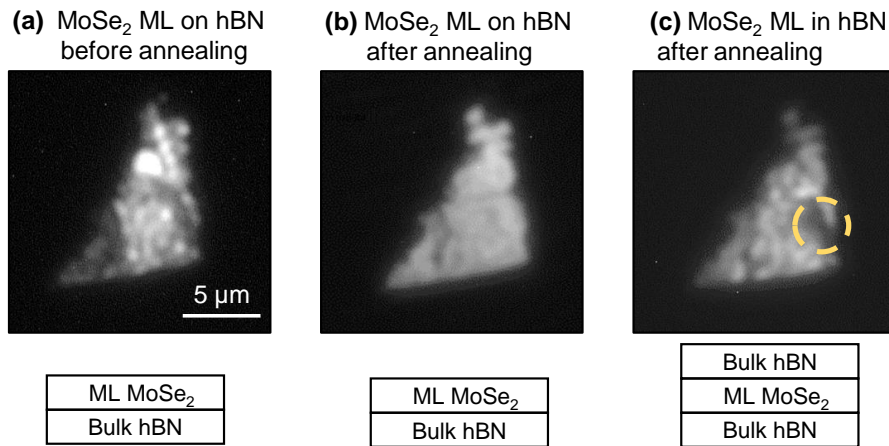


Figure 3.11: (a) PL-image of MoSe₂ / hBN before and in (b), after annealing protocol. The sample homogeneity drastically increased. Wrinkles and bright local areas disappear. By the pressure performed on the sample, a crack in the monolayer appeared. Remaining visible anomaly is attributed to accumulated water residues and other trapped molecules, as well as to local disorder of the crystal structure. (c) PL-image after encapsulation in hBN and repeated annealing. The second transfer process induced again multiple defects which still emerge after annealing. The cryogenic measurements of the region marked with the yellow dashed circle showed the most unperturbed spectrum, which indicates that most bright emission originates from sample disorder. Pictures are modified in brightness for better spatial clarity and therefore do not allow a direct intensity comparison.

Spectroscopy of tungsten based transition metal dichalcogenides

The model introduced in chapter 2.3 sets the emission spectra of TMD monolayer in the new context of phonon sidebands. For this application, a lifetime limited resolution is needed. As described in chapter 3.1.2, recent publications have shown narrow full width at half maximum (FWHM) linewidths of encapsulated TMD monolayers near the radiative limit. Encapsulation thereby means, embedding the monolayer in the dielectric environment of hexagonal boron nitride (hBN). Resulting heterostructures are of the form hBN / ML / hBN.

4.1 Encapsulated samples

At first, the resulting fit procedure was used on spectral signatures from the group of Prof. Urbaczek, extracted from references [15, 35]. Emission spectra of a gated sample of encapsulated WSe₂ (schematically shown in figure 4.1 (c)) and a non-gated encapsulated WS₂ sample are analyzed, where both show narrow spectral line-widths at the lifetime limit. Gated samples facilitate control over the free charge carriers inside the sample via an externally applied voltage. Trions are quasi particles similar to excitons, where two electrons or holes form a bound state with their counterpart. With control over the intrinsic doping level, the sample is tuned to charge neutrality, which suppresses trion states. Exclusion of the trion states reduces the number of radiative processes and therefore enables a first application of the model. Inclusion of trion states into the framework of momentum-dark excitons is an ongoing process and will not be discussed in this work.

In figures 4.1 (a) and (b), the cryogenic emission spectrum of the gated and encapsulated WSe₂ ML is shown. Four separate peaks appear in the range of 1.67 eV to 1.74 eV. To address these peaks, the band structure of WSe₂, with all its momentum-direct and indirect exciton configurations, is considered as described in chapter 2.3.2. The energetically highest peak can be referred to as the bright

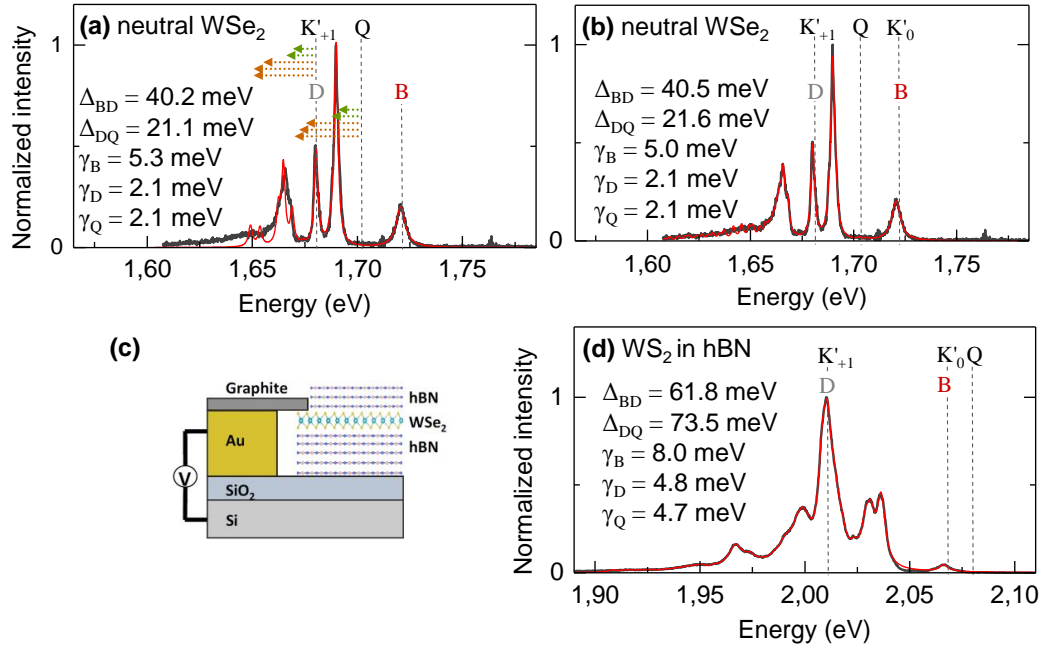


Figure 4.1: **(a)** Emission spectra at 4 K of a gated sample of encapsulated WSe₂ tuned to charge neutrality. Data extracted from [15] is displayed in black and model fit from first-order phonon replicas of momentum-dark Q- and K'₊₁ excitons in red. The energetic position of the spin-bright (B) and spin-dark (D) states together with the K'₊₁- and Q valley are indicated by the dashed lines. The energetic position of acoustical (optical) phonon replicas are illustrated by the green (orange) arrows. Resulting fit parameters are displayed, where the main result is the experimental extraction of Δ_{BD} . **(b)** Refined model fit, including momentum-dark excitons from K'₀ and allowing for higher order Γ phonon replicas. **(c)** Schematic depiction out of [15], showing the gated hBN / WSe₂ ML / hBN heterostructure. **(d)** Emission spectra from an encapsulated WS₂ ML obtained from [35]. In contrast to WSe₂, the energetic position of the momentum-dark Q-exciton configuration is above the bright state. Acoustical phonon sidebands from Q deform the bright state and optical phonon replicas are reproducing the doublet between the B and D state.

state B (labeled in red) and corresponds to the momentum direct transition at the K valley. The peak at ~ 1.68 eV is labelled as the spin-dark state D (grey), as in previous discussions.

The origin of the brightest peak at ~ 1.69 eV as well as the most red peak at ~ 1.665 eV have not yet been identified. With the inclusion of momentum-dark excitons and associated phonon replicas from the Q and K'₊₁ valleys all peaks

are addressed. The spectrum is reproduced by addition of single Lorentzian functions, one for each phonon replica and two for the momentum-direct transitions B and D. The phonon energies are taken from reference [20] and are allowed to vary by ± 2 meV to account for sample specific variations in strain or dielectric environment. Raman shifts from sample to sample variations are commonly observed in a similar range. The energy differences Δ_{BD} and Δ_{DQ} are fit parameters. The Q_{+1} and Q'_0 exciton configurations, as well as the D and the K'_{+1} states are assumed to be energetically degenerate by neglecting electron-hole exchange interactions. In figure 4.1 (a), only first order phonon replicas from the K'_{+1} and Q valleys were considered, where the scattering processes from K'_0 are omitted. This results in 12 Lorentzians corresponding to five possible phonon processes from two momentum-dark excitons and two direct transitions. This spectral decomposition identifies the brightest peak as a replica of acoustic phonons originating from the Q valley. The peak below the zero phonon line of D arises from a combination of acoustic sidebands of Q excitons and of optical replicas of K'_{+1} . The best fit is obtained for $\Delta_{BD} = 40.2$ meV and $\Delta_{DQ} = 21.1$ meV. The accordance of the fit with the prominent peaks indicates that the energetic ordering of the states in a single particle description does not change with excitonic corrections. Equal lifetime limited timescales are assumed for all phonon assistant decay channels. The best fit was obtained at $\gamma_B = 5.3$ meV and $\gamma_Q = \gamma_D = 2.1$ meV for all momentum-dark states. Smaller linewidths for momentum-dark states are consistent with long-lived states that have no direct radiative decay channel. This first order spectral analysis, however, clearly fails to reproduce the low energy wing of the spectrum.

For this reason, the fitting procedure was refined and the resulting fit is shown in figure 4.1 (b). Scattering processes from the K'_0 valley are included as well as higher-order phonon replicas mediated by additional Γ -phonons. As phonons from the Γ point have zero momentum contribution to the scattering process, arbitrary high orders of scattering processes are possible. These higher order radiative channels reproduce the red shoulder of the spectrum as well as the most red peak. Similar values are obtained for Δ_{BD} and Δ_{DQ} , as well as very little variation in the linewidths.

Figure 4.1 (d) shows the PL-spectrum of encapsulated WS_2 with no active charge control. The main difference compared to the previous sample is the energetic position of the Q exciton manifold, which is slightly above the bright state. The corresponding acoustic sidebands deform the B peak and the three optical sidebands contribute the apparent doublet between the D and B states. The Lorentzian fit, displayed in red, includes higher order processes from K'_0 , K'_{+1} and Q, reproducing the spectrum on a full scale. The resulting fit parameters are consistent

with the single particle bandstructure. Spin-orbit splitting between the lowest two CB states yields $\Delta_{BD} = 61.8$ meV and the energetic position of the Q valley, determined experimentally by the fit parameter, $\Delta_{DQ} = 73.5$ meV. The resulting linewidths are $\gamma_B = 8.0$ meV, $\gamma_D = 4.8$ meV and $\gamma_Q = 4.7$ meV. Slight variations of the fit originate from the omitted trion contribution to this PL spectrum. On the other hand, the very good agreement with the data indicates a low intrinsic doping level.

The spectral analysis presented above determines the energetic position of the Q valley from an experimental approach. Publications which report on spectral signatures of encapsulated WSe₂ [21, 31, 34, 40, 42, 47] were revisited by this group in order to test the stability of the model for sample specific deviations. The resulting fit procedures show a variation in Δ_{BD} and Δ_{DQ} on the order of 2 meV. The resulting phonon amplitudes, on the other hand, show strong sample specific variations. Crystal disorder induced by the fabrication methods used heavily impact the amplitude distribution of the phonon sidebands. This leads to a deviation from the intuitive assumption that higher order processes necessarily have a smaller spectral contribution. Another limitation of this analysis is the afore mentioned negligence of exchange effects. The assumption of degenerate energetic positions of K'_{+1} and K'_0 with the D and B states is not necessarily justified. The same applies to the constraint of keeping the h^+ in the K valley of the VB. Disregarding the acoustic ZA-mode as well as the optical modes E'' and A''_1 also impacts the accuracy of our analysis. Furthermore, assuming identical linewidths for every phonon process is a supplemental simplification. The e^- -scattering rates differ in each mode, depending on the e^- energy. Taking the electron wave vector k to be along the K- Γ axis, timescales for scattering processes vary from 10^{-11} s to 10^{-14} s, whereas the exciton lifetimes can limit all possible scattering mechanisms. Further analysis of resulting phonon amplitudes and comparison to theoretical estimates of the scattering rates, with the lifetimes of resulting virtual intermediate states, exceeds the scope of this work.

Despite the limitations of our model, the analysis of encapsulated ML with narrow linewidths clearly validates the taken approach. Not only can the full spectrum be accurately reproduced, but the resulting fit parameters also stay in good agreement with recently determined energy positions of the D state. The same goes for theoretical predictions of the energetic ordering of the CB states [22, 35].

4.2 Monolayer on hexagonal boron nitride

After confirmation of the model through application to linewidths near the lifetime limit, the analysis is expanded to uncapped tungsten-based MLs on top of hBN. Cryogenic confocal photoluminescence spectroscopy is carried out with the setup described in chapter 3.2. The samples are fabricated with the transfer method shown in 3.1.3, where the WS_2 / hBN sample was subsequently annealed and the WSe_2 / hBN sample was directly measured without annealing. Spectra in black as well as the model fit in red are displayed in figure 4.2.

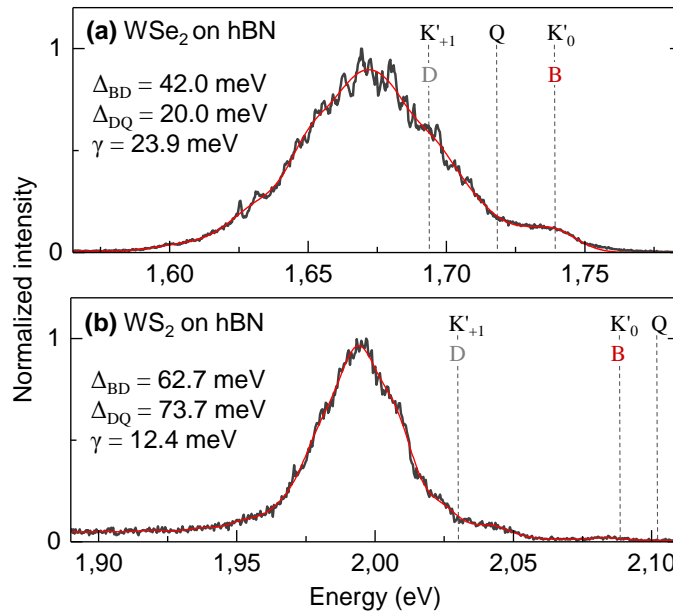


Figure 4.2: **(a)** Cryogenic spectra of ML WSe_2 transferred on top of hBN. Inhomogeneous broadening limits the analysis due to the strongly reduced resolution. The spectral contribution of only one acoustic (LA) and one optical (A_1) phonon-mediated scattering process is taken into account. **(b)** Emission spectra of WS_2 on hBN, where the transversal optical (TO) mode is also included. The samples differ in the fabrication process, where WS_2 was additionally annealed after transfer - a potential explanation for the strongly reduced linewidth.

The WSe_2 sample was excited with a 635 nm cw laser at a power of $70 \mu\text{W}$. The resulting spectrum in 4.2 (a) shows a very broad emission in the range from 1.5 eV to 1.8 eV with no distinct sub-peaks. The high energy shoulder of the spectrum is assigned to the excitonic emission of the bright state. The overall blue shift of the emission by ~ 20 meV, compared to the encapsulated sample is attributed

to differences in the effective dielectric environment. On the one hand, the contrast in linewidth compared to the encapsulated samples is a strong indication that the spectral signature is dominated by surface effects. On the other hand, the observed inhomogeneous broadening of the peaks has multiple origins and displays a lack in sample quality. Strain applied on the crystal structure during the transfer process, sample specific disorder of the crystal, residues from the fabrication process as well as local potential deformations from inhomogeneous charge distributions limit the sample quality. The latter plays a major role as this sample was not annealed. Trapped water molecules between the interfaces influence dipolar excitonic emission owing to their intrinsic dipole moment.

Due to inhomogeneous broadening of the emission spectrum Gaussian functions, rather than Lorentzians, are used to reproduce the emission spectra. The FWHM linewidths of all associated radiative channels are set equal and were found to be $\gamma = 23.9$ meV, which reduces the number of resolvable phonon processes. Thus, only one acoustic (LA) and one optical (A_1) phonon mode is taken into account. Higher order processes from these modes are included. The best fit is obtained for $\Delta_{BD} = 42.0$ meV and $\Delta_{DQ} = 20.0$ meV.

The WS_2 / hBN sample is excited with pulsed excitation provided by a commercial white-light laser source (SuperK extreme, NKT) tuned to 532 nm, with a repetition rate of 78 MHz, spectral band of 6 nm and a power of 70 μ W. As displayed in figure 4.2 (b), the bright state is mapped to the most blue broad peak at ~ 2.07 eV, in good agreement with literature [14]. Identical to the WSe_2 sample, the total blue shift results from changes in the effective dielectric environment. The fit procedure is again limited by the broad inhomogeneous linewidths observed. Only the LA, TO and A_1 mode are taken into account. The best fit parameters are $\gamma = 12.4$ meV, $\Delta_{BD} = 62.7$ meV and $\Delta_{DQ} = 73.7$ meV.

Interestingly, both WX_2 / hBN samples show a spectral blue shift compared to the encapsulated samples. Revisiting the simple excitonic hydrogen model described in chapter 2.2, one could expect the opposite. As the observed spectra have $E = E_{gap} - E_X$, with $E_X \sim 1/\epsilon^2$, a reduction of the effective dielectric constant ϵ should lead to an increase in exciton binding energy and therefore, to a reduction of the photon energy. However, in the case of 2D semiconductors the strong Coulomb interactions lead to an electric field which propagates mostly in the surrounding dielectric environment. Therefore, the renormalization of the single particle bandgap exceeds the reduction in binding energy and is the dominant process. Recent reflection measurements on WS_2 with different dielectric bottom layers confirm this statement [30].

The resulting Gaussian fits obtained for the two samples are in good agreement with the data. In total, 20 (37) Gaussian functions were used to fit the spectra of the WSe₂ (WS₂) sample. Slight variations arise from the trion exclusion, which cannot be neglected in the presence of intrinsic doping. Simplifications concerning exchange effects can be safely neglected, due to the broad FWHM linewidths. These furthermore enforce a reduction of allowed phonon processes. The resulting values for the fit parameters, however, have to be viewed skeptically as the fit procedure is bound to constraints. The fit parameters are the energetic positions of the B and D states, the position of the Q valley as well as the spectral linewidth. The energetic position of the bright peak is chosen by manual extraction of the most blue peak position, where anti-Stokes scattering processes are neglected due to the cryogenic temperatures of the environment. The linewidths were set to be above 15 meV for WSe₂, in order to fully match the B state peak. For WS₂, they were bound to lie between 5 meV and 15 meV. Assuming a negligible change in Δ_{BD} by the bandgap renormalization via variation of effective dielectric environment justifies setting the bounds close to the values obtained by the Lorentzian fit, see 4.1. A further analysis of the sample introduces another option for fixing the dark state energy to a small interval, discussed below.

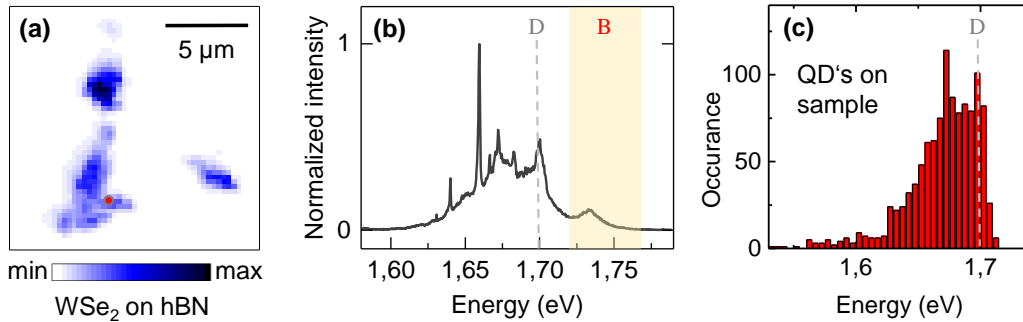


Figure 4.3: **(a)** Hyper-spectral map of the WSe₂ ML on hBN, where the pixel values are mapped to an integrated intensity of the bright state. The color bar is white for minimum and black for maximum intensity. The sample contains many spatial positions, where QD emission marks the spectral signature. The red dot marks an exemplary spatial position, with the spectrum shown in **(b)**, where the yellow region shows the integrated range of the hyper-spectral map. The energetic distribution of QD emission found in the sample is shown in the histogram displayed in **(c)**. The onset of QD occurrence at 1.7 eV corresponds with the proposed energetic position of the dark state.

Figure 4.3 (a) shows a hyperspectral map of the WSe₂ / hBN sample, recorded with the use of a commercial piezo-scanner from Attocube (operated with DC-

voltage). Excitation is provided by a cw diode laser at 635 nm, with a power of 70 μ W. Pixel values correspond to the integrated intensity in the region of the bright state, which is 1.72 eV to 1.77 eV. Corresponding values are color-coded in white for zero and black for maximum intensity. Position specific variations originating from different hBN-terraces result in a spectral shift within the sample. Previously discussed impurities lead to the broad FWHM peaks of the fit and give rise to an inhomogeneous intensity distribution. The sample was found to contain many positions with characteristic quantum dot (QD) emission, where one exemplary position (marked by the red dot) is displayed in figure 4.3 (b). The spectral band of the bright state, used for the hyperspectral map, is marked in yellow. Spectral signatures from QDs are visible at ~ 1.7 eV and ~ 1.66 eV. Peak analysis of the full sample results in an energetic distribution of QD emission, shown in the histogram displayed in figure 4.3 (c). Most prominent is the sharp onset of the peak close to 1.7 eV, the proposed energetic position of the spin-dark state D.

QDs are mostly found in the border regions of the flake, where the exfoliation process produced major crystal deformations and defects. Such potential deformations of the crystal induce localized excitonic states by selectively lowering the bandgap. The emission of such states lies energetically below all momentum-direct radiative decay channels. Therefore, the onset indicates the energetic position of the D state close to 1.7 eV, as it is the lowest lying momentum-direct state for WSe_2 . This consolidates the Δ_{BD} values obtained for WSe_2 and justifies that the influence of renormalization on Δ_{BD} is neglected for WS_2 . This insight is translated to the relative energetic position of the Q valley. The boundaries of the fit allow Q to vary by 7 meV around the obtained values from encapsulated samples, where an accordance to the encapsulated samples is found on the scale of 1 meV.

The different FWHM of the linewidths from the two samples is noticeable and can be attributed to the varying production steps, where the WS_2 sample was additionally annealed after transfer. The resulting smaller linewidths, may be material specific. However, this strongly indicates a reduction of dipolar water residues between the surfaces and therefore, less Coulomb interactions of the exciton with its surrounding charge carriers, leading to a reduction of the observed inhomogeneous broadening. For that reason, annealing after each transfer process is established for the following heterostructure of encapsulated MoSe_2 .

Spectroscopy of encapsulated molybdenum diselenide

In contrary to the tungsten-based TMDs discussed in the previous section, molybdenum-based MLs have an inverse spin ordering and therefore no contribution from the spin dark momentum-direct exciton configuration. With the exclusion of the Q valley, the bandstructure is fully dominated by the K and K' points of the first Brillouin zone. In this chapter, we expand the model of phonon replicas to the spectral signatures of encapsulated MoSe₂.

The hBN / MoSe₂ / hBN sample was fabricated by repetitive use of the transfer method discussed in chapter 3.1.3, with subsequent annealing after each transfer. PL imaging was used to record this process regarding sample quality and the results are shown in figure 3.11. The yellow dashed circle points towards the position on the sample with narrow spectral linewidths, which are discussed in the following and displayed in figure 5.1.

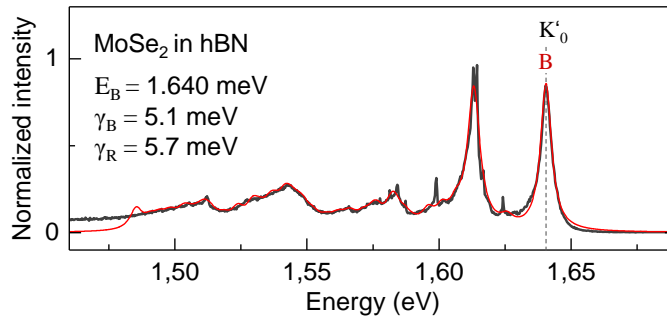


Figure 5.1: Emission spectrum at 4 K of encapsulated MoSe₂, displayed in black. Decomposition of the spectrum into contributions from neutral excitons is marked in red. The sharp features are attributed to quantum dots and therefore excluded from the fit procedure. Optical phonon replicas arising from momentum-dark K' ₀ excitons reproduce the peak around 1.61 eV, commonly referred to as trion emission. Higher order phonon processes up to fourth order reprint the repetitive features of the red shoulder to a high degree.

The sample was examined at a cryogenic temperature of 4.2 K and excitation was provided by a continuous wave (cw) diode laser at 532 nm with a power of 3.7 μ W. The two most prominent peaks are typical for ML emission of MoSe₂, where in literature, the peak at 1.64 eV comes from the excitonic emission of the spin bright state. The peak at 1.61 eV is assigned to the spectral signature of the trion contribution. The observed red shoulder with its sub-peak structure, is commonly assigned to localized states, arising from disorder. However, a refined analysis without trion inclusion is carried out, accounting for possible momentum-dark excitons from the K'₀ valley and higher order scattering processes with Γ -phonons. The result reproduces the emission spectrum to a very high degree.

The sharp peaks at 1.60 eV and 1.625 eV are attributed to quantum dot emission and are therefore manually excluded from the analysis. The fit contains 51 Lorentzian functions corresponding to one spin-bright state and five possible phononic modes (see chapter 2.3.1) with K-momentum. Higher order processes up to fourth order are implemented, involving up to three Γ phonons. The LO $_{\Gamma}$ and TO $_{\Gamma}$ modes are energetically closer than 1 meV and are therefore not resolved. The highest amplitude of the implemented replicas is contributed from the A_{1K} optical mode, with an energy shift of 25.6 meV, +1.7 meV from the fit constrains. This very accurately matches the suggested energetic position of the trion [37].

The existence of a trion state is not in question, as the amplitude of this peak is dependent on the substrate doping level and shows sensitivity to laser induced doping effects [8]. However, inclusion of trion states in the model is not mandatory. Energetically indistinguishable phonon replicas question the overall amplitude contribution of the trion state.

All phonon replicas are set to an identical FWHM linewidth with fit constraints ranging from 2 meV to 10 meV, resulting in $\gamma_R = 5.7$ meV. The direct transition of the spin bright (B) exciton has an independent linewidth of $\gamma_B = 5.1$ meV. The errors in linewidth are $\sim 3\%$. According to Fermi's golden rule, the emission linewidth scales inversely with the lifetime of the excited state. Interestingly, the replicas show a slightly shorter lifetime than the momentum-direct transition of the B state. In contrast, the replicas of the high-quality samples discussed in chapter 4.1 show an inverse behaviour, thus a longer lifetime than the direct transitions. This discrepancy is naively attributed to the exclusion of the trion state in MoSe₂. Momentum-dark trion states will produce a similar comb of phonon sidebands and thereby reduce the spectral width of the involved peaks. Additional lifetime measurements promise to bring more insight. Assigning the same linewidth to all replicas despite the number of participant phonons, however, is

a strong simplification and may distort the results obtained.

The red shoulder with its sub-peak structure is a very sample-specific feature which is absent in many reports [1, 8]. The fit procedure however, accurately reproduces the red shoulder with its repetitive signature up to the order of the Γ -processes taken into account. It is therefore individual crystal deformation which tunes the weight of the phonon sideband amplitudes and this has yet to be understood in more detail.

The main discrepancy of the fit to the data is found at the spectral region next to the bright state. A possible explanation is the exclusion of the Q valley from this model. A report on density functional theory estimated the Q valley to be only 28 meV above the K valley in the conduction band [20]. Thus, the energetic region around the bright state is reached with phonon replicas arising from K-Q momentum-dark excitons as the phonon energy of different modes lies between 13.3 meV and 37.5 meV.

The question of the trion contribution for ungated samples therefore remains and can be delegated to future measurements, where reflection contrast measurements for example show a promising approach to probe the direct transitions of the crystal.

Summary and outlook

Spectral analysis of monolayer TMDs in varying dielectric environments was presented in this work. Due to the narrow spectral linewidths of encapsulated ML a profound investigation of phonon replicas originating from momentum-dark excitoninc states was possible. A model was introduced which aims to reproduce all spectral signatures of the most prominent TMDs.

The experimental starting point of this work was the exfoliation of bulk crystal, carried out for the four most prominent TMDs: MoS_2 , MoSe_2 , WS_2 and WSe_2 . By means of direct exfoliation onto silicon substrates, monolayers were randomly produced, with no control over their position. For this reason, a stamping stage was built in order to implement a deterministic transfer technique, enabling the production of heterostructures.

The layer thickness of exfoliated flakes was quantified using complementary methods. Raman spectroscopy was employed to measure layernumber-dependent modes in few-layer crystals on a silicon substrate. Additionally, an optical setup was modified for the purpose of PL-imaging, enabling spatial resolution. The layernumber of exfoliated TMDs on a transparent PDMS stamp, required for the transfer technique, was determined by intensity. This approach also allowed quality characterization of the ML and was therefore established to monitor the sample fabrication at multiple stages. Finally, the optical contrast of images from a reflection microscope was analyzed and compared to the results of previous methods. Fixed illumination conditions allow fast and reliable layernumber quantification.

Sample annealing indicated a reduction of disorder and was therefore implemented after each transfer process. Hexagonal boron nitride was exfoliated in the same way as the TMD crystals and was used as a dielectric substrate. WSe_2 and WS_2 MLs were transferred onto hBN and afterwards, optical experiments were carried out using confocal spectroscopy at cryogenic temperatures. Furthermore, a successful encapsulation of ML MoSe_2 was shown and analyzed in optical experiments.

A model of phonon replicas, arising from possible momentum-dark exciton for-

mations lies at the core of this work. At first, the resulting fit procedure was used on emission spectra extracted from references [35, 15]. Lifetime limited spectral linewidths of a gated WSe₂ ML, encapsulated in hBN and tuned to charge neutrality were investigated. The trion states were excluded. Peaks were attributed to a spin bright, a spin dark state as well as to acoustic and optical phonon sidebands arising from the momentum-dark states. The relative energetic position of the Q valley was determined by spectral decomposition. Next, the analysis was carried out on an encapsulated WS₂ ML, where the spectrum was reproduced without the inclusion of a trion state.

The analysis was then expanded to the fabricated heterostructures in this work, consisting of ML on top of hBN. These samples show inhomogeneous broadened emission spectra. Even though bandgap renormalization leads to an overall shift in PL-energy, no relative change in energy between the valleys was found. Further investigation of quantum dots revealed the energetic position of the lowest-lying radiative state and confirmed the results obtained by the fit procedure.

Finally, the model was expanded to MoSe₂ and the spectral signature of an encapsulated ML was fitted. Acoustic and optical phonon replicas from the K' valley can fully reproduce all spectral features, including the trion state. A repetitive, defect mediated sub-peak structure in the red shoulder is fully captured by higher order phonon sidebands. The energetic correspondence of the trion peak to an optical phonon replica from the K' valley questions the contribution of the trion to the observed peak.

Lifetime limited linewidths are the basis for further investigations. As the samples produced in this work only locally show FWHM linewidths of at best 5 meV, the observed spectral signatures are still dominated by disorder. A more advanced transfer method is needed, where the "hot-pick up technique" described in reference [29] promises a reduction of transfer residues. Furthermore, gated structures are essential to analyze the trion contribution to the spectra. The analysis in this work does not consider restrictions from electron-phonon scattering rates or optical selection rules. A widely accepted underlying model is needed to exclude the strong energy variations for optical transitions found in theory and experiments. With that, the approach of this work can be embedded in a theoretical framework and applied to open questions.

Bibliography

- [1] Obafunso A. Ajayi et al. “Approaching the Intrinsic Photoluminescence Linewidth in Transition Metal Dichalcogenide Monolayers”. In: *arXiv:1702.05857* (2017).
- [2] Lindlau et al. “Identifying optical signatures of momentum-dark excitons in monolayer transition metal dichalcogenides”. In: *in preparation* (2017).
- [3] B. Arnaud et al. “Huge Excitonic Effects in Layered Hexagonal Boron Nitride”. In: *Physical Review Letters* 96.2 (Jan. 18, 2006). ISSN: 0031-9007, 1079-7114.
- [4] Timothy C. Berkelbach, Mark S. Hybertsen, and David R. Reichman. “Theory of neutral and charged excitons in monolayer transition metal dichalcogenides”. In: *Physical Review B* 88.4 (July 25, 2013). ISSN: 1098-0121, 1550-235X. DOI: [10.1103/PhysRevB.88.045318](https://doi.org/10.1103/PhysRevB.88.045318).
- [5] K. S. Bhargavi, Sukanya Patil, and S. S. Kubakaddi. “Acoustic phonon assisted free-carrier optical absorption in an n-type monolayer MoS₂ and other transition-metal dichalcogenides”. In: *Journal of Applied Physics* 118.4 (July 28, 2015), p. 044308. ISSN: 0021-8979, 1089-7550.
- [6] Sheneve Z. Butler et al. “Progress, Challenges, and Opportunities in Two-Dimensional Materials Beyond Graphene”. In: *ACS Nano* 7.4 (Apr. 23, 2013), pp. 2898–2926. ISSN: 1936-0851, 1936-086X.
- [7] F. Cadiz et al. “Excitonic linewidth approaching the homogeneous limit in MoS₂ based van der Waals heterostructures : accessing spin-valley dynamics”. In: *arXiv* (Feb. 1, 2017). arXiv: [1702.00323](https://arxiv.org/abs/1702.00323).
- [8] Fabian Cadiz et al. “Ultra-low power threshold for laser induced changes in optical properties of 2D molybdenum dichalcogenides”. In: *2D Mater.* 3.4 (2016), p. 045008. ISSN: 2053-1583.
- [9] Ting Cao et al. “Valley-selective circular dichroism of monolayer molybdenum disulphide”. In: *Nat Commun* 3 (June 6, 2012), p. 887. ISSN: 2041-1723. DOI: [10.1038/ncomms1882](https://doi.org/10.1038/ncomms1882).
- [10] G. Cassaboïs, P. Valvin, and B. Gil. “Hexagonal boron nitride is an indirect bandgap semiconductor”. In: *Nat Photon* 10.4 (Apr. 2016), pp. 262–266. ISSN: 1749-4885. DOI: [10.1038/nphoton.2015.277](https://doi.org/10.1038/nphoton.2015.277).
- [11] A Castellanos-Gomez, N Agraït, and G Rubio-Bollinger. “Optical identification of atomically thin dichalcogenide crystals”. In: *Applied Physics Letters* 96.21 (May 24, 2010), p. 213116. ISSN: 0003-6951, 1077-3118. DOI: [10.1063/1.3442495](https://doi.org/10.1063/1.3442495).
- [12] Andres Castellanos-Gomez et al. “Deterministic transfer of two-dimensional materials by all-dry viscoelastic stamping”. In: *2D Materials* 1.1 (Apr. 4, 2014), p. 011002. ISSN: 2053-1583. DOI: [10.1088/2053-1583/1/1/011002](https://doi.org/10.1088/2053-1583/1/1/011002).

- [13] Jianyi Chen et al. “Chemical Vapor Deposition of High-Quality Large-Sized MoS₂ Crystals on Silicon Dioxide Substrates”. In: *Adv. Sci.* 3.8 (Aug. 1, 2016). ISSN: 2198-3844. DOI: [10.1002/advs.201600033](https://doi.org/10.1002/advs.201600033).
- [14] Alexey Chernikov et al. “Exciton Binding Energy and Nonhydrogenic Rydberg Series in Monolayer WS₂”. In: *Physical Review Letters* 113.7 (Aug. 13, 2014). ISSN: 0031-9007, 1079-7114. DOI: [10.1103/PhysRevLett.113.076802](https://doi.org/10.1103/PhysRevLett.113.076802).
- [15] E. Courtade et al. “Charged excitons in monolayer WSe₂: experiment and theory”. In: *arXiv* (May 5, 2017). arXiv: [1705.02110](https://arxiv.org/abs/1705.02110).
- [16] A. K. Geim and K. S. Novoselov. “The rise of graphene”. In: *Nat Mater* 6.3 (Mar. 2007), pp. 183–191. ISSN: 1476-1122. DOI: [10.1038/nmat1849](https://doi.org/10.1038/nmat1849).
- [17] M. M. Glazov et al. “Spin and valley dynamics of excitons in transition metal dichalcogenide monolayers”. In: *Phys. Status Solidi B* 252.11 (Nov. 1, 2015), pp. 2349–2362. ISSN: 1521-3951. DOI: [10.1002/pssb.201552211](https://doi.org/10.1002/pssb.201552211).
- [18] Dheeraj Golla et al. “Optical thickness determination of hexagonal Boron Nitride flakes”. In: *Applied Physics Letters* 102.16 (Apr. 22, 2013), p. 161906. ISSN: 0003-6951, 1077-3118. DOI: [10.1063/1.4803041](https://doi.org/10.1063/1.4803041).
- [19] Yuan Huang et al. “Reliable Exfoliation of Large-Area High-Quality Flakes of Graphene and Other Two-Dimensional Materials”. In: *ACS Nano* 9.11 (Nov. 24, 2015), pp. 10612–10620. ISSN: 1936-0851. DOI: [10.1021/acs.nano.5b04258](https://doi.org/10.1021/acs.nano.5b04258).
- [20] Zhenghe Jin et al. “Intrinsic transport properties of electrons and holes in monolayer transition-metal dichalcogenides”. In: *Physical Review B* 90.4 (July 24, 2014). ISSN: 1098-0121, 1550-235X. DOI: [10.1103/PhysRevB.90.045422](https://doi.org/10.1103/PhysRevB.90.045422).
- [21] Aaron M. Jones et al. “Optical generation of excitonic valley coherence in monolayer WSe₂”. In: *Nat Nano* 8.9 (Sept. 2013), pp. 634–638. ISSN: 1748-3387. DOI: [10.1038/nnano.2013.151](https://doi.org/10.1038/nnano.2013.151).
- [22] Andor Kormányos et al. “k - p theory for two-dimensional transition metal dichalcogenide semiconductors”. In: *2D Mater.* 2.2 (2015), p. 022001. ISSN: 2053-1583. DOI: [10.1088/2053-1583/2/2/022001](https://doi.org/10.1088/2053-1583/2/2/022001).
- [23] Liangbo Liang and Vincent Meunier. “First-principles Raman spectra of MoS₂, WS₂ and their heterostructures”. In: *Nanoscale* 6.10 (Apr. 23, 2014), pp. 5394–5401. ISSN: 2040-3372. DOI: [10.1039/C3NR06906K](https://doi.org/10.1039/C3NR06906K).
- [24] Yuxuan Lin et al. “Dielectric Screening of Excitons and Trions in Single-Layer MoS₂”. In: *Nano Lett.* 14.10 (Oct. 8, 2014), pp. 5569–5576. ISSN: 1530-6984. DOI: [10.1021/nl501988y](https://doi.org/10.1021/nl501988y).

- [25] Xiaoze Liu et al. “Strong light matter coupling in two-dimensional atomic crystals”. In: *Nat Photon* 9.1 (Jan. 2015), pp. 30–34. ISSN: 1749-4885. DOI: [10.1038/nphoton.2014.304](https://doi.org/10.1038/nphoton.2014.304).
- [26] M. R. Molas et al. “Brightening of dark excitons in monolayers of semiconducting transition metal dichalcogenides”. In: *2D Mater.* 4.2 (2017), p. 021003. ISSN: 2053-1583. DOI: [10.1088/2053-1583/aa5521](https://doi.org/10.1088/2053-1583/aa5521).
- [27] Andre Neumann et al. “Opto-valleytronic imaging of atomically thin semiconductors”. In: *Nat Nano* (Jan. 16, 2017). ISSN: 1748-3387. DOI: [10.1038/nnano.2016.282](https://doi.org/10.1038/nnano.2016.282).
- [28] Maurizia Palummo, Marco Bernardi, and Jeffrey C. Grossman. “Exciton Radiative Lifetimes in Two-Dimensional Transition Metal Dichalcogenides”. In: *Nano Lett.* 15.5 (May 13, 2015), pp. 2794–2800. ISSN: 1530-6984. DOI: [10.1021/nl503799t](https://doi.org/10.1021/nl503799t).
- [29] Filippo Pizzocchero et al. “The hot pick-up technique for batch assembly of van der Waals heterostructures”. In: *Nature Communications* 7 (June 16, 2016), p. 11894. ISSN: 2041-1723. DOI: [10.1038/ncomms11894](https://doi.org/10.1038/ncomms11894).
- [30] Archana Raja et al. “Coulomb engineering of the bandgap in 2D semiconductors”. In: *arXiv* (Feb. 3, 2017). arXiv: [1702.01204](https://arxiv.org/abs/1702.01204).
- [31] S Schwarz et al. “Electrically pumped single-defect light emitters in WSe₂”. In: *2D Materials* 3.2 (June 27, 2016), p. 025038. ISSN: 2053-1583. DOI: [10.1088/2053-1583/3/2/025038](https://doi.org/10.1088/2053-1583/3/2/025038).
- [32] Malte Selig et al. “Excitonic linewidth and coherence lifetime in monolayer transition metal dichalcogenides”. In: *Nature Communications* 7 (Nov. 7, 2016), p. 13279. ISSN: 2041-1723. DOI: [10.1038/ncomms13279](https://doi.org/10.1038/ncomms13279).
- [33] Philipp Tonndorf et al. “Photoluminescence emission and Raman response of monolayer MoS₂, MoSe₂, and WSe₂”. In: *Opt. Express*, OE 21.4 (Feb. 25, 2013), pp. 4908–4916. ISSN: 1094-4087. DOI: [10.1364/OE.21.004908](https://doi.org/10.1364/OE.21.004908).
- [34] Philipp Tonndorf et al. “Single-photon emission from localized excitons in an atomically thin semiconductor”. In: *Optica* 2.4 (Apr. 20, 2015), pp. 347–352. ISSN: 2334-2536. DOI: [10.1364/OPTICA.2.000347](https://doi.org/10.1364/OPTICA.2.000347).
- [35] G. Wang et al. “In-plane Propagation of Light in Transition Metal Dichalcogenide Monolayers: Optical Selection Rules”. In: *arXiv* (Apr. 18, 2017). arXiv: [1704.05341](https://arxiv.org/abs/1704.05341).
- [36] Qing Hua Wang et al. “Electronics and optoelectronics of two-dimensional transition metal dichalcogenides”. In: *Nat Nano* 7.11 (Nov. 2012), pp. 699–712. ISSN: 1748-3387. DOI: [10.1038/nnano.2012.193](https://doi.org/10.1038/nnano.2012.193).

- [37] Jakob Wierzbowski et al. "Direct exciton emission from atomically thin transition metal dichalcogenide heterostructures near the lifetime limit". In: *arXiv* (2017).
- [38] Neil R. Wilson et al. "Determination of band offsets, hybridization, and exciton binding in 2D semiconductor heterostructures". In: *Science Advances* 3.2 (Feb. 2017). ISSN: 2375-2548. DOI: [10.1126/sciadv.1601832](https://doi.org/10.1126/sciadv.1601832).
- [39] Di Xiao et al. "Coupled Spin and Valley Physics in Monolayers of MoS₂ and Other Group-VI Dichalcogenides". In: *Physical Review Letters* 108.19 (May 7, 2012). ISSN: 0031-9007, 1079-7114. DOI: [10.1103/PhysRevLett.108.196802](https://doi.org/10.1103/PhysRevLett.108.196802).
- [40] Tengfei Yan et al. "Exciton valley dynamics in monolayer WSe₂ probed by the two-color ultrafast Kerr rotation". In: *Phys. Chem. Chem. Phys.* 19.4 (2017), pp. 3176–3181. ISSN: 1463-9076, 1463-9084. DOI: [10.1039/C6CP07208A](https://doi.org/10.1039/C6CP07208A).
- [41] Mingxiao Ye et al. "Recent advancement on the optical properties of two-Dimensional molybdenum Disulfide thin films". In: *Photonics* 2.1 (Mar. 16, 2015), pp. 288–307. DOI: [10.3390/photonics2010288](https://doi.org/10.3390/photonics2010288).
- [42] Yumeng You et al. "Observation of biexcitons in monolayer WSe₂". In: *Nature Physics* 11.6 (May 11, 2015), pp. 477–481. ISSN: 1745-2473, 1745-2481. DOI: [10.1038/nphys3324](https://doi.org/10.1038/nphys3324).
- [43] Long Yuan and Libai Huang. "Exciton dynamics and annihilation in WS₂ 2D semiconductors". In: *Nanoscale* 7.16 (Apr. 9, 2015), pp. 7402–7408. ISSN: 2040-3372. DOI: [10.1039/C5NR00383K](https://doi.org/10.1039/C5NR00383K).
- [44] Xiao-Xiao Zhang et al. "Magnetic brightening and control of dark excitons in monolayer WSe₂". In: *Nature Nanotechnology* (June 26, 2017). ISSN: 1748-3387, 1748-3395. DOI: [10.1038/nnano.2017.105](https://doi.org/10.1038/nnano.2017.105).
- [45] Xin Zhang et al. "Phonon and Raman scattering of two-dimensional transition metal dichalcogenides from monolayer, multilayer to bulk material". In: *Chem. Soc. Rev.* 44.9 (2015), pp. 2757–2785. ISSN: 0306-0012, 1460-4744. DOI: [10.1039/C4CS00282B](https://doi.org/10.1039/C4CS00282B).
- [46] Weijie Zhao et al. "Lattice dynamics in mono- and few-layer sheets of WS₂ and WSe₂". In: *Nanoscale* 5.20 (Sept. 27, 2013), pp. 9677–9683. ISSN: 2040-3372. DOI: [10.1039/C3NR03052K](https://doi.org/10.1039/C3NR03052K).
- [47] You Zhou et al. "Probing dark excitons in atomically thin semiconductors via near-field coupling to surface plasmon polaritons". In: *Nature Nanotechnology* (June 26, 2017). ISSN: 1748-3387, 1748-3395. DOI: [10.1038/nnano.2017.106](https://doi.org/10.1038/nnano.2017.106).

-
- [48] Bairen Zhu, Xi Chen, and Xiaodong Cui. “Exciton Binding Energy of Monolayer WS_2 ”. In: *Sci Rep* 5 (Mar. 18, 2015). ISSN: 2045-2322. DOI: [10 . 1038 / srep09218](https://doi.org/10.1038/srep09218).
- [49] C. R. Zhu et al. “Strain tuning of optical emission energy and polarization in monolayer and bilayer MoS_2 ”. In: *Physical Review B* 88.12 (Sept. 9, 2013). ISSN: 1098-0121, 1550-235X. DOI: [10 . 1103 / PhysRevB . 88 . 121301](https://doi.org/10.1103/PhysRevB.88.121301).

Danksagung

Hier habe ich letztlich die Gelegenheit mich für die wunderbare Zeit in der Arbeitsgruppe von Prof. Högele am Lehrstuhl Kotthaus zu bedanken. Vielen Dank für all die Geduld und Nachsicht, für scheinbare Immunität gegenüber sich wiederholenden Fragen und für Ansprechpersonen für alle Anliegen. Danke Alex für einen tieferen Einblick in die Welt von Quasi-Teilchen und ebenso für die angenehm flache Hierarchie die du betreibst. Besonderer Dank geht an Micahel Föerg, der zeitgleich mit seinem neugeborenen Kind auch noch mich "Rookie" zu betreuen hatte. Denke daran - be raptor - shoot laser - kill robots. Ebenso möchte ich den Doktoranden Jonathan Noé und Manuel Nutz für tolle Filmabende und Biergartengespräche danken. Auch Jessica Lindlau danke ich ganz herzlich für die produktive Zusammenarbeit und die regelmäßige Erinnerungen an den Zustand des Labors. Letztendlich geht mein Dank an meine hochschwangere Freundin Anna die mich rundum unterstützt hat und mir täglich Motivation gab. Danke auch Isi für die vielen Stunden, die du dir Zeit genommen hast. Meinen ungeborenen Sohn möchte ich sagen: Danke dass du nicht früher raus wolltest. Wir freuen uns auf dich. Ach und du solltest auf jeden Fall studieren, es lohnt sich.

Selbstständigkeitserklärung

Hiermit erkläre ich, die vorliegende Arbeit selbstständig verfasst zu haben und keine anderen als die in der Arbeit angegebenen Quellen und Hilfsmittel benutzt zu haben.

München,

Victor Funk